Available on the CMS information server **CMS NOTE AN-13-064**

The Compact Muon Solenoid Experiment

CMS Draft Note

Mailing address: CMS CERN, CH-1211 GENEVA 23, Switzerland

2013/07/18
Head Id:
Archive Id: 196952M
Archive Date: 2013/06/28
Archive Tag: trunk

Search for a standard-model-like Higgs boson in the decay channel $\mathrm{H} \rightarrow \mathrm{ZZ} \rightarrow 2\ell 2\mathrm{q}$ at $\sqrt{s} = 8$ TeV

A. De Cosa (*U. & INFN-Napoli*), F. Fabozzi (*U. Basilicata & INFN-Napoli*), D. Bortoletto, M. Kress, M. Vidal (*Purdue U.*), M. Yalvac (*Middle East Technical U.*), Y.J. Lu, S.S. Yu (*National Central U.*), L. K. Saini (*Panjab U.*), S. Bolognesi, A. Whitbeck (*Johns Hopkins U.*), M. Mozer (*KIT*), K. Kanishchev (*INFN-Padova*), G. Codispoti, J. Fernández de Trocóniz (*U. Autonoma de Madrid*), and D. Domínguez, O. González, J.M. Hernández, E. Navarro, P. Garcia-Abia (*CIEMAT-Madrid*)

Abstract

A search for a standard-model-like Higgs boson decaying into two Z bosons with subsequent decay into two leptons and two quark-jets, $\mathrm{H} \rightarrow \mathrm{ZZ} \rightarrow \ell^+\ell^-\mathrm{q}\bar{\mathrm{q}}$ is performed. The analysis uses 19.6 fb^{-1} of data collected by the CMS experiment from proton-proton collisions produced in LHC at $\sqrt{s} = 8$ TeV. The analysis exploits the kinematic information and the flavor tagging of the leading particles of the event in order to isolate hypothetical Higgs boson signals with mass values in the range from 230 GeV/c^2 to 650 GeV/c^2. No evidence of a Higgs boson signal is found and upper limits are set on the Higgs boson production cross section in that mass range.

1 Introduction

The Higgs mechanism is an essential element of the Standard Model (SM) of particles and their interactions explaining the origin of mass and playing a key role in the Physics of electroweak symmetry breaking. A suitable Higgs boson candidate, predicted by the Higgs mechanism, has recently been found with a mass around 126 GeV [1, 2]. However, many models predict more than a single boson, such as the SM-Higgs boson field mixing with a yet unknown scalar with higher mass or scenarious with a second Higgs doublet as they appear in supersymmetric theories. Thus we present here further searches for Higgs like particles using the SM Higgs as a benchmark model.

The CMS collaboration is performing searches for the Higgs boson in several decay modes. This comprehensive effort aims at gaining sensitivity over a large range of Higgs boson masses, M_{H}, by combining many different analyses. We expect that this effort will explore the region with $M_{\mathrm{H}} \geq 2m_{\mathrm{Z}}$ with a sensitivity to that reaches far beyond SM Higgs production cross sections.

In this note we report a study of the search for a Higgs-like boson in $\mathrm{H} \rightarrow \mathrm{ZZ}$ when one of Z decays as $\mathrm{Z} \rightarrow \ell^{+}\ell^{-}$ (where ℓ is either electron or muon) and the other as $\mathrm{Z} \rightarrow \mathrm{q\bar{q}}$, using LHC proton-proton collision data at $\sqrt{s} = 8$ TeV. The analysis is performed by studying the mass of the ZZ system, $M_{\ell\ell jj}$, which is expected to exhibit a narrow peak for hypothetical signals at low M_{H}, significantly increasing at high M_{H}. The dominant background process is Z+jets production from Drell-Yan processes, with smaller contributions from top-quark decays and from diboson events. Unlike for the signal, the $M_{\ell\ell jj}$ distribution of the background events is not resonant, providing a useful handle to isolate signal events. The analysis exploits the kinematic information and the flavor tagging of the leading particles of the event to enhance a hypothetical signal over the contamination. Data from a signal-free control region are used to normalize and tune the dominant Drell-Yan plus jets background reducing the dependence on the simulation. The contamination from $\mathrm{t\bar{t}}$ events is directly extracted from data. A similar analysis [3] was performed by CMS using data at $\sqrt{s} = 7$ TeV.

2 Data and simulated samples

The analysis uses data from proton-proton collisions produced in the LHC at a centre-of-mass energy, $\sqrt{s}$, of 8 TeV, with an integrated luminosity of 19.6 fb^{-1}.

The data, collected by the CMS experiment in the data taking campaign of year 2012, are reconstructed using the official CMS software CMSSW, release 5_3_X. Data of the various data taking periods are packed into different primary datasets according to the signatures of particles and jets (physics objects) identified by the high level trigger (HLT). Several of these primary datasets are used in order to cover the final states expected in the $\mathrm{H} \rightarrow \mathrm{ZZ} \rightarrow \ell^{+}\ell^{-}\,\mathrm{q\bar{q}}$ processes and to perform dedicated background studies (details in appendix A).

Only data that pass the strict quality requirements imposed by the CMS central certification team are used in the analysis (more technically, the latest available reprocessings and official JSON files are utilized for each data taking period).

Official samples of simulated events (MC), produced in the Summer12 simulation campaign, are used in order to study the properties of the Higgs boson events (for M_{H} values in the range 230 GeV/c^{2} to 650 GeV/c^{2}) and of the background processes. These samples are also reconstructed with the official software CMSSW, release 5_3_X.

The available signal samples of different M_{H} values are listed in appendix A along with the cross-sections times branching fraction of the process $\mathrm{H} \to \mathrm{ZZ} \to \ell^{+}\ell^{-}\,\mathrm{q\bar{q}}$. The H production cross section and the $\mathrm{H} \to \mathrm{ZZ}$ branching fraction are provided as function of the Higgs boson mass by the LHC Higgs cross section working group [4, 5]. The branching ratio of the Z boson into pairs of leptons (e, μ and τ) and quarks are taken from the PDG [6]. The samples are generated using the POWHEG [7] event generation program.

The samples of background simulated events are displayed in appendix A, together with their cross section (calculated at NLO and NNLO [8] dependending on the process) and equivalent luminosity.

To characterize the dominant Drell-Yan background both inclusive and parton-exclusive Z+jets samples are used, produced with the MadGraph [9] event generator imposing a high mass of the dilepton pair ($M_{\ell\ell} > 50\,\mathrm{GeV}$). The background from top events is due mainly to $\mathrm{t\bar{t}}$ events, for whose study a $\mathrm{t\bar{t}} \to 2l2\nu2b$ sample is produced using POWHEG. Diboson events from standard model processes are simulated with inclusive ZZ, WZ, and WW samples using Pythia [10].

All the events in the analysis, either data or simulated, are processed with the official CMS tools for analysis (PAT) to ensure standard object definitions (particle flow objects). The common skim of the CMS H2l2q analysis team is described in [11].

3 Event reconstruction

The signature of Higgs boson signal events is a lepton pair and a quark pair, each with an invariant mass around the Z boson mass. The invariant mass of the $\ell^{+}\ell^{-}\mathrm{q\bar{q}}$ system, $M_{\ell\ell jj}$, is consistent with the mass of a hypothetical Higgs boson and is used as the main observable to discriminate signal events from background events.

Particles are reconstructed in CMS using a particle flow algorithm from the electronic signals they leave in the detector. Leptons (electrons [12] and muons [13]) and jets [14, 15] are selected imposing quality criteria to ensure high efficiency in their reconstruction and identification, and good momentum and mass resolutions.

Data events used in the analysis belong to the *DoubleMu* and *DoubleElectron* primary datasets, which are built from the un-prescaled triggers `HLT_Mu17_Mu8` (*DoubleMu*) and `HLT_Ele17_CaloIdT_TrkIdVL_CaloIsoVL_TrkIsoVL_Ele8_CaloIdT_TrkIdVL_CaloIsoVL_TrkIsoVL` (*DoubleElectron*), among other un-prescaled and prescaled triggers. The event selection requirements of the analysis are tighter than those of the trigger. More details on the trigger strategies for Higgs boson searches are in [16].

To avoid dependence on the details of the trigger emulation no trigger requirements are imposed on simulated events. Instead, event weights are assigned to simulated events according to the probabilities of leptons to pass the trigger (detailed in appendix B). The trigger efficiency tables for leptons are computed in bins of (p_{T}, η) from data using a tag-&-probe technique. We have checked that the trigger simulation yields similar efficiencies. See discussion in appendix B.

The identification of $\mathrm{Z} \to \mathrm{e^{+}e^{-}}$, $\mathrm{Z} \to \mu^{+}\mu^{-}$, and $\mathrm{Z} \to \mathrm{q\bar{q}}$, is a crucial step of the analysis. Leptonic decays of Z bosons are built from same-flavour opposite-charge lepton pairs, which satisfy lepton identification criteria. Hadronic Z boson decays are made of pairs of jets. Leptons and jets are required to fulfill additional kinematic constraints, described later.

Electrons are reconstructed with the GSF algorithm [17]. In order to ensure good electron reconstruction, the electron supercluster is required to be inside the ECAL acceptance volume ($|\eta| < 2.5$) and outside the ECAL barrel-endcap overlap region ($1.4442 < |\eta| < 1.566$). They must satisfy the standard *loose working point* of the cut-based electron identification for 2012 analyses [18]. Muons are reconstructed by both the GlobalMuon and the particle flow muon reconstruction algorithms and are required to lie in the acceptance region $|\eta| < 2.4$. They must satisfy the standard *tight working point* of the cut-based muon identification for 2012 analyses [19]. The precise electron and muon identification cuts are detailed in appendix C. They comprise identification and isolation criteria and, specifically for electrons, conversions rejection requirements.

In the particle flow algorithm, lepton isolation is defined as the sum of p_{T} or E_{T} deposits of charged and neutral hadrons, and photons, computed in a ΔR cone around the lepton direction. To ensure independence of the isolation from the number of pile-up interactions and to reduce the probability of jets to overlap with the cone, a standard recipe recommended by the e-gamma and muon POGs is used. For electrons, the overall pile-up energy contribution is estimated as the average energy density in the event multiplied by an effective area, using the recommended cone size $\Delta R < 0.3$. For muons, the recommended DeltaBeta correction with $\Delta R < 0.4$ is applied.

The lepton identification efficiencies are evaluated from data using a standard tag-&-probe method, which requires the reconstruction of the dilepton system with invariant mass in the range [60-120] GeV/c^2. Appendix C provides details of the tag-&-probe method and the scale factors for electron and muon selection requirements, which are very close to 1.

The $\mathrm{Z} \to \mathrm{e}^+\mathrm{e}^-$ and $\mathrm{Z} \to \mu^+\mu^-$ candidates are constructed from leptons with momenta $p_{\mathrm{T}} >$ 40 GeV/c (leading lepton) and $p_{\mathrm{T}} > 20$ GeV/c (subleading lepton). Z decays into leptons are accepted for subsequent analysis if the $\ell^+\ell^-$ invariant mass lies within $[76, 106]$ GeV/c^2 (Figure 1). Not being included the state-of-the-art lepton calibrations originates visible differences in the $M_{\ell^+\ell^-}$ distributions in data and simulations. Reweighting the simulated events to match the peak position and resolution in data has a tiny impact in the signal efficiency, less than 0.2%. The $M_{\ell^+\ell^-}$ resolution is around 10% better in the simulation than in data. The correction of this difference has a negligible impact in the $M_{\ell\ell jj}$ distributions, largely dominated by the dijet resolution.

The particle flow jets are reconstructed with the anti-k_T algorithm [20] with radius parameter $R = 0.5$. In order to obtain high reconstruction efficiency and precise energy measurements, jets are required to be inside the tracker acceptance, $|\eta| < 2.4$. Jet energy corrections are applied to data and simulated events [21]. The so-called Fastjet algorithm [22] applies L1 energy corrections to account for pile-up. Jets originating from pile-up interactions are removed requiring jets to be taggable [23] and $\beta > 0.2$ (Figure 2), where β is the sum of transverse momenta of the charged particles in the jet coming from the primary vertex normalized to the sum of transverse momenta of all the charged particles in the jet. Jets must have $p_T > 30\,\mathrm{GeV}/c$ to form $\mathrm{Z} \to \mathrm{q\bar{q}}$ candidates, which rejects fake candidates with low-p_{T} jets from QCD background. The invariant mass distribution of $\mathrm{Z} \to \mathrm{q\bar{q}}$ candidates is displayed in Figure 3.

4 Event selection

The $\mathrm{Z} \to \ell^+\ell^-$ and $\mathrm{Z} \to \mathrm{q\bar{q}}$ decays are combined into $\ell^+\ell^- jj$ candidates, labeled Higgs boson candidates. To avoid double counting of the same object reconstructed in different collections (for instance, leptons inside a jet) the angular separation of isolated leptons and jets is required

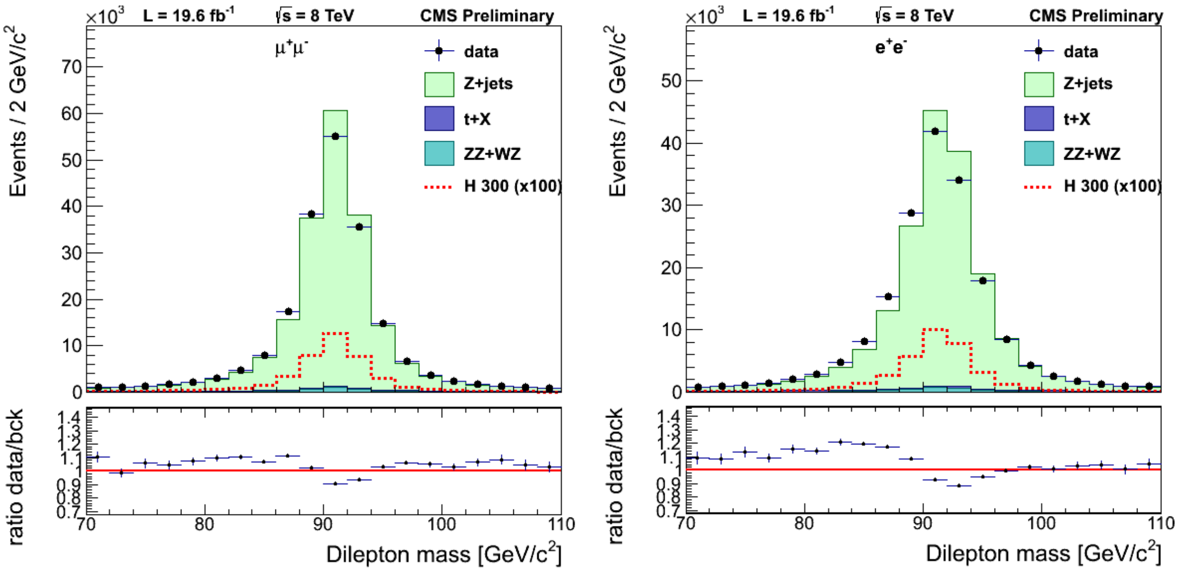

Figure 1: Dilepton invariant mass in data and simulation of $Z \to \ell^+\ell^-$ candidates after lepton selection cuts for muons (left) and electrons (right). The background distributions are normalized to data.

to be $\Delta R = \sqrt{\Delta\phi^2 + \Delta\eta^2} > 0.5$. In the following, the entire selection procedure described above is referred to as "preselection" of $\ell^+\ell^- jj$ candidates. These preselection criteria are detailed in table 1. Appendix D contains the p_T distributions of leptons and jets after preselection cuts.

Table 1: Preselection requirements.

observable	selection criterion
lepton quality	see section 3
jet quality	see section 3
same lepton flavor, opposite charge	
$p_T(l^{\pm})$	$> 40/20$ GeV/c
p_T(jets)	> 30 GeV/c
$\lvert\eta\rvert(\ell^{\pm})$	$(e^{\pm}) < 2.5$, $(\mu^{\pm}) < 2.4$
$\lvert\eta\rvert$(jets)	< 2.4
jet β	> 0.2
ΔR	> 0.5

In order to suppress the dominant Drell-Yan Z+jets background and contamination from $t\bar{t}$ events, $\ell^+\ell^- jj$ candidates are selected in the m_{jj} region $[71, 111]$ GeV/c^2, called signal region. Outside of this signal region, candidates with m_{jj} within $[60, 130]$ GeV/c^2 are used for background determination. This is the so-called sideband region.

Due to the relatively large branching fraction of the Z-bosons decaying into a pair of bottom-antibottom quarks, compared to the abundance of light-quark or gluon jets in Z+jets background events, the *Jet Probability* b-tagging algorithm [24] is used to identify jets originating from heavy-flavour quarks. No selection of candidates is performed based on btagging probabilities. Rather, events are clasified into three exclusive categories: 2-, 1-, and 0-btag. The 2-btag category includes events with one jet tagged using JPM (medium working point of the JP algorithm) and another jet tagged using JPL (loose working point). The 1-btag category in-

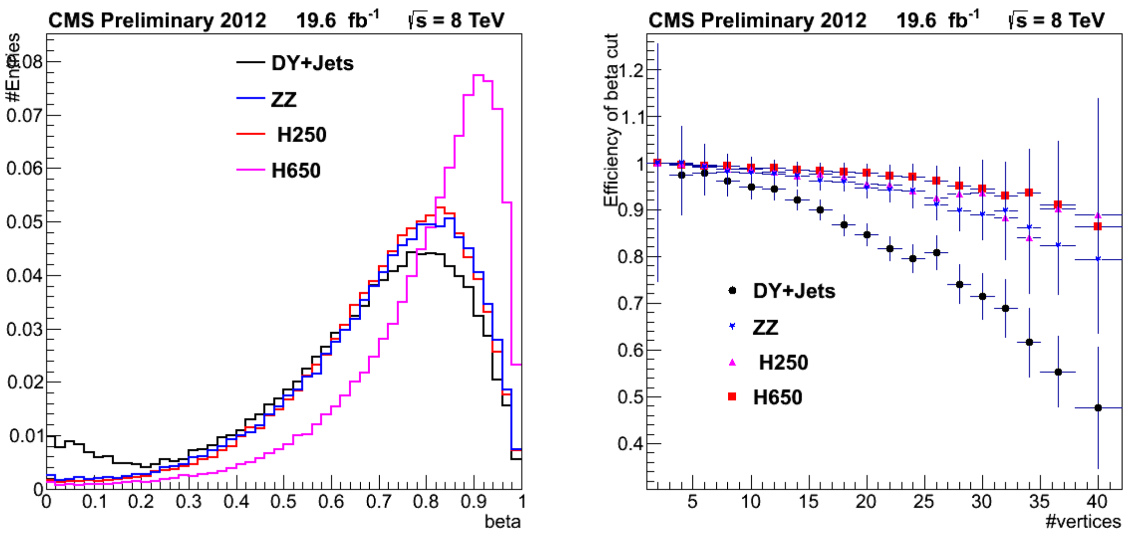

Figure 2: Left: jet β distribution for signal, Z+jets background and $t\bar{t}$ events. Right: efficiency of the β cut as function of the number of reconstructed vertices, for signal and Z+jets background.

cludes events with at least one jet tagged using JPL. The untagged events belong to the 0-btag category. The different signal-to-background ratio of each category helps improving the sensitivity of the analysis. The methods used to estimate the backgrounds are common to all the categories.

Using simulated Drell-Yan Z+jets events, the average b-tagging efficiencies $\langle \epsilon_i^{MC} \rangle$ and scale factors $\langle \mathrm{SF}_i \rangle$ are obtained for jets in events passing selection cuts. The scale factors are calculated, using the Moriond13 prescription, for b, c, and light jets separately. The average tagging efficiencies in the data are calculated as the product of the average tagging efficiencies for MC and the corresponding average scale factors: $\langle \epsilon_i \rangle = \langle \epsilon_i^{MC} \rangle \cdot \langle \mathrm{SF}_i \rangle$, $i = b,\ c$, light. For b and c jets these average data tagging effiencies are used. In the case of light jets (ℓ, mistags), data mistag rates were provided by the Btag POG in 2011, as a function of jet p_T and $|\eta|$. To take into account the jet p_T and $|\eta|$ dependence, the average data mistag rate using the 2011 prescription $\langle \epsilon_\ell^{2011} \rangle$ was calculated as well, defining $\epsilon_\ell(p_T, |\eta|) = \epsilon_\ell^{2011}(p_\mathrm{T}, |\eta|)\, \langle \epsilon_\ell \rangle / \langle \epsilon_\ell^{2011} \rangle$. The values of $\langle \epsilon_\ell \rangle / \langle \epsilon_\ell^{2011} \rangle$ are 1.126 (1.089) for JPL (JPM) mistags.

The Higgs boson candidate is selected among those in the M_{jj} signal region that pass all the selection criteria. When no candidate survives the selection cuts in the signal region, the Higgs boson candidate is chosen from the candidates in the sideband. The event is rejected whenever no candidates are found in either region. In less than 3% of the events after final selection there is more than one Higgs boson candidate per event. In these cases, the candidate in the highest btag category is selected. If more than one candidate remains, the one with minimum $|M_{\ell^+\ell^-} - m_\mathrm{Z}| + |M_{jj} - m_\mathrm{Z}|$ is chosen.

There are several features in the signal $H \to ZZ \to 2l2j$ decay kinematics which discriminate it against background. These kinematic differences are exploited to optimize the selection and maximize the signal significance. Five helicity-dependent angular observables fully describe kinematics in the decay $2 \to 1 \to 2 \to 4$ as in $ab \to X \to ZZ \to 2l2q$ [25, 26]. They are orthogonal to the three invariant masses of the X and the two Z bosons. Longitudinal and transverse momenta of the X are also additional orthogonal observables and could be used in analyses, but they typically have weaker discrimination power and rely on modeling of the

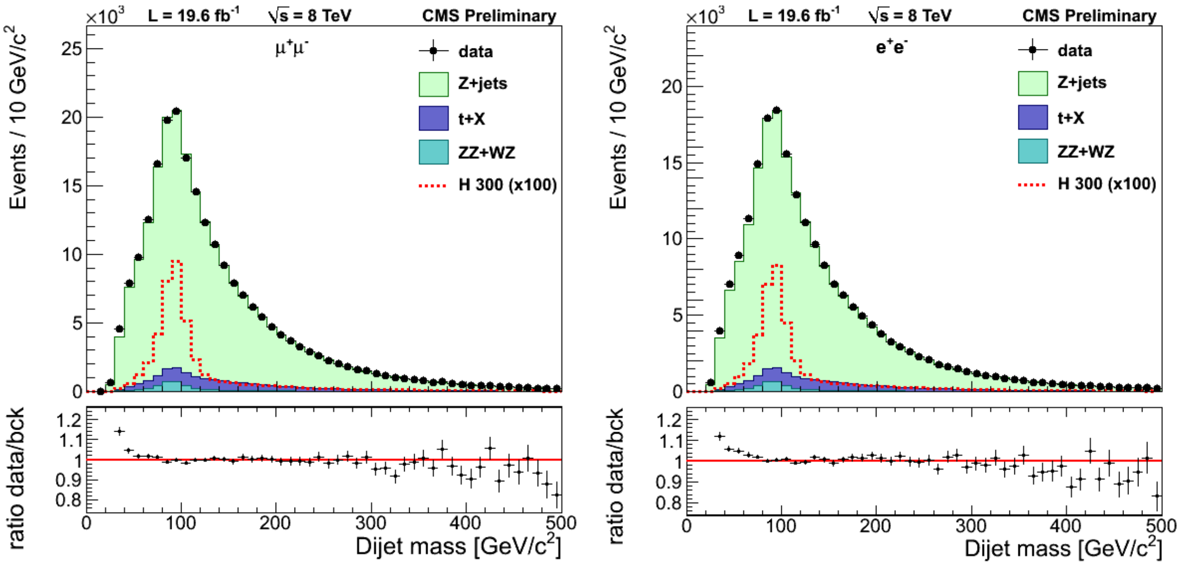

Figure 3: Dijet invariant mass in data and simulations for $Z \to q\bar{q}$ candidates for events with dimuons (left) and dielectrons (right) after preselection cuts. The background distributions are normalized to data.

PDFs and process dynamics. The above orthogonal observables are largely uncorrelated and are more attractive to be used in event selection rather than raw kinematic observables.

The diagram on Figure 4 illustrates the production and decay chain $ab \to X \to ZZ \to 2\ell 2q$, which is a function of three helicity angles θ_1, θ_2, and Φ, and two production angles θ^* and Φ_1. Parameterization of both signal and background distributions have been derived and implemented in [25, 27]. A linear likelihood discriminant, LD, is constructed from the signal and background probabilities defined using the five angles. Signal sensitivity is improved requiring events with $LD > 0.5$, a selection cut almost optimal for the three btag categories. A comparison of angular distribution in data and simulation is presented in Figure 5 (after all selection cuts but the LD cut) and Figure 6 (after final selection) for events with e^+e^- and $\mu^+\mu^-$ combined. Good agreement is appreciated, except in the low LD region dominated by background. A cross-check detailed in appendix E demonstrates that the disagreement at low LD values is due to a bad modeling of the $\cos\theta^*$ distribution for Z+jets events at $|\cos\theta^*| > 0.85$, which has a negligible impact on the signal.

An important background in the 2 b-tag category originates from $t\bar{t}$ decays, which contain two true b-quark jets (Figure 7 (left)). This background is reduced requiring a particle flow missing E_T significance [28] less than 10 (Figure 7 (right)) (applied to the three btag categories). Small differences in the MET significance of the data and the Drell-Yan Z+jets simulation are taken into account studying the region MET significance < 6, where the contamination of the t+X background is reduced. It is observed that a simple multiplicative factor of 1.15 ± 0.01 brings the MC distribution in very good agreement with the data, a factor that is stable for muons and electrons, and as a function of the number of vertices in the event. The validity of this factor has been checked up to larger values of the MET significance in a top-depleated data subsample, requiring $p_T(\ell\ell jj) < 20$ GeV/c. Therefore the MET significance in the Drell-Yan, diboson and Higgs boson MC events is multiplied by a factor 1.15. The effect of this factor on the efficiency of the cut MET significance is minimal (in all cases the efficiency changes by less than 1%).

Selection cuts for the final analysis are listed in table 3, identical for the three b-tag categories.

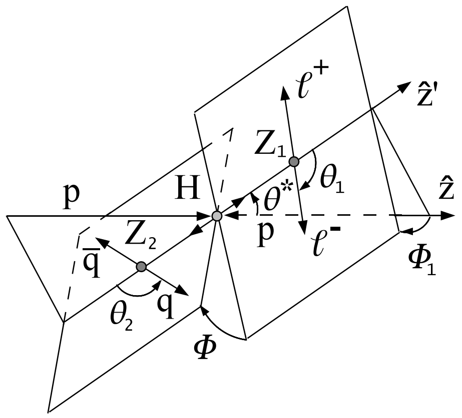

Figure 4: Diagram depicting the decay $X \to ZZ \to 2l2q$ and the 5 angles which describe such a decay.

Figure 8 displays the numbers of events after each cut for the data and the background simulation. The efficiency of each cut is listed in Table 2.

Table 2: Relative and cumulative efficiencies of the cuts for the data and the background simulation.

	data		H (300 GeV/c^2)		Z+jets		Diboson		t+X	
cut	rel.	cumul.	rel.	cumul.	rel.	cumul.	rel.	cumul.	rel.	cumul.
presel.	1.00	1.00	1.00	1.00	1.00	1.00	1.00	1.00	1.00	1.00
$m_{\ell\ell}$	0.85	0.85	0.94	0.94	0.93	0.93	0.86	0.86	0.22	0.22
LD	0.53	0.45	0.84	0.79	0.54	0.51	0.58	0.50	0.75	0.17
MET sig.	0.97	0.44	0.99	0.78	0.99	0.50	0.95	0.47	0.40	0.07
m_{jj}	0.29	0.13	0.65	0.51	0.29	0.15	0.57	0.27	0.32	0.02

The expected numbers of signal and background events in the electron and muon channels, in the $M_{\ell\ell jj}$ range [160, 800] GeV/c^2, are listed for 19.6 fb^{-1} in table 4. Appendix F details the contributions of the various background sources in the mass range $[M_{\mathrm{H}} - 6\%, M_{\mathrm{H}} + 10\%]$, for different M_{H} values.

Table 3: Selection requirements in the three btag categories.

observable	0 btag	1 btag	2 btag
btag	none	JPL	JPM & JPL
$m_{\ell\ell}$	[76,106] GeV/c^2		
m_{jj}	[71,111] GeV/c^2		
helicity LD	> 0.5		
missing E_{T} significance	< 10		

5 Background determination

After the event selection described in section 4, the following SM processes are considered as background in this analysis: diboson, Z+jets, and $\mathrm{t\bar{t}}$ production.

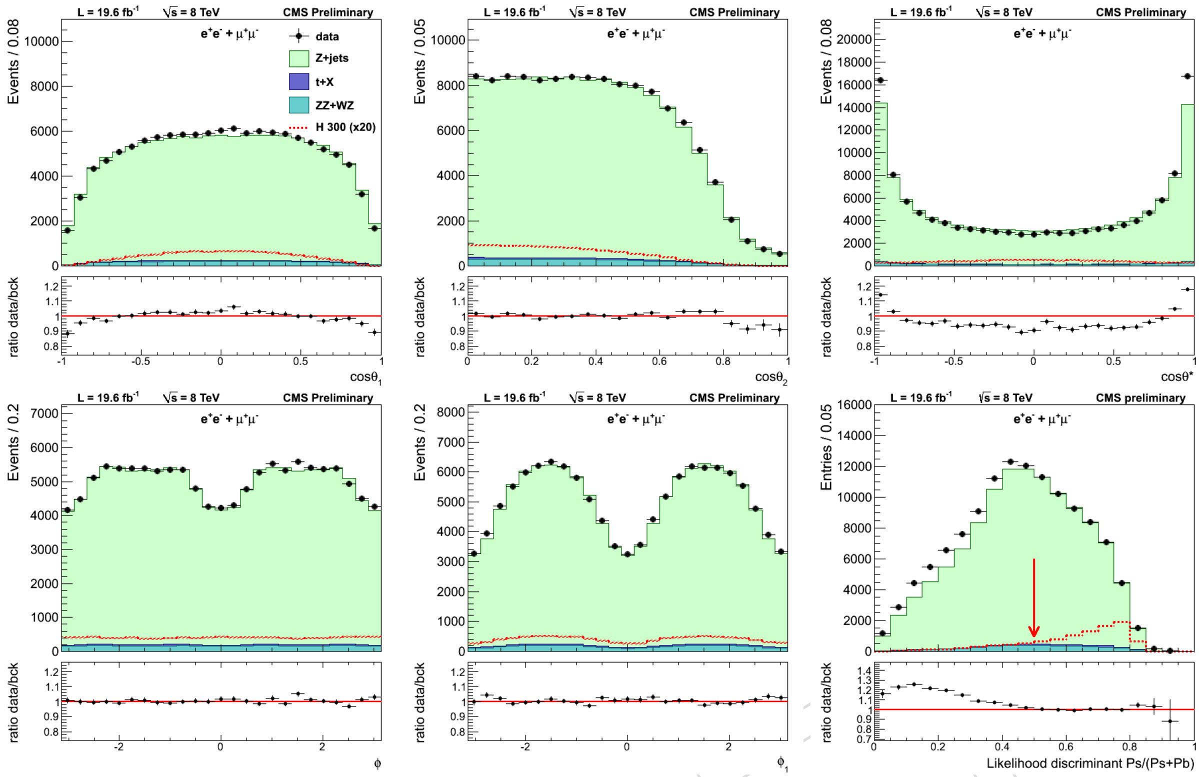

Figure 5: Distributions of the five helicity angles and the likelihood discriminant, LD, after final selection except for the cut LD > 0.5, for 2012 data (points with error bars) and simulated samples (histograms). The red dashed histogram indicates 20 times the expected distribution for a 300 GeV/c^2 mass Higgs boson. The distributions of the background are normalized to the data, except the LD distribution which is normalized to the data with LD > 0.5.

Table 4: Expected and observed yields with 19.6 fb^{-1} of data. The expected background is composed of p_T-weighted simulated Z+jets, data-driven top+X and diboson MC. The background is normalized to the data in the m_{jj} sideband.

	0 btag		1 btag		2 btag	
	$\mu^+\mu^- jj$	$e^+e^- jj$	$\mu^+\mu^- jj$	$e^+e^- jj$	$\mu^+\mu^- jj$	$e^+e^- jj$
expected background	14809	13490	5478	4786	525	440
observed data	14697	13312	5458	4819	522	461
M_H (GeV/c^2)	signal expectation					
250	110.6	100.8	55.8	51.1	18.4	16.9
300	124.4	112.3	66.6	57.0	24.5	21.0
400	121.9	107.2	68.2	60.4	27.4	24.1
500	57.0	52.1	33.4	29.9	13.8	12.3
600	21.7	19.7	13.2	11.9	5.4	4.9

The diboson production (mainly ZZ and WZ) is simulated using MC while the other two contributions are estimated either using MC simulation corrected to data in control regions (Z+jets), or extracted directly from data in control regions ($t\bar{t}$). The latter two cases are described in detail in the following subsections.

A weight depending on the number of simulated vertices is applied to MC simulated events in order to match the pilue-up distribution of the data. Figure 9 displays the comparison of the number of reconstructed vertices in data and MC, which shows an excellent agreement.

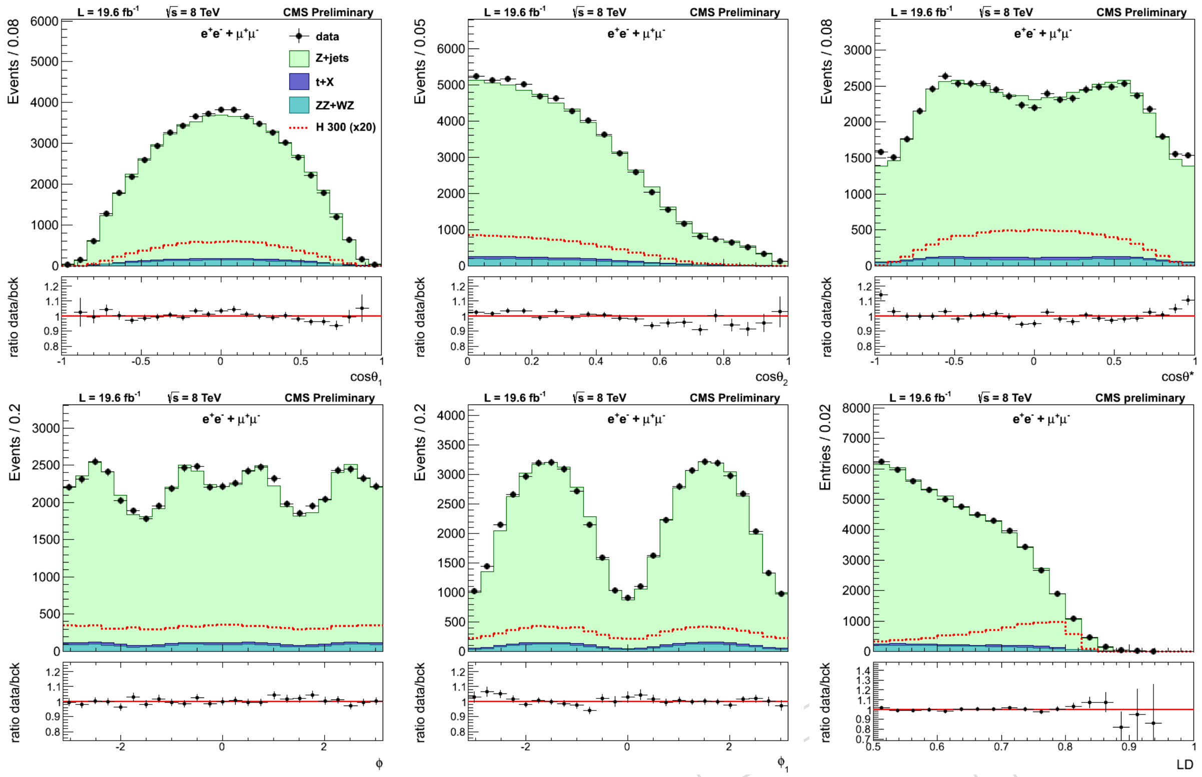

Figure 6: Distributions of the five helicity angles after final selection for 2012 data (points with error bars) and simulated samples (histograms). The red dashed histogram indicates 20 times the expected distribution for a 300 GeV/c^2 mass Higgs boson. The distributions of the background are normalized to the data with LD > 0.5.

Drell-Yan Z+jets contamination

Most events in the selected $\ell^+\ell^-\mathrm{q\bar{q}}$ sample come from Drell-Yan Z+jets processes. A real Z boson decaying into $\ell^+\ell^-$ and a number of high p_{T} jets may easily yield signal-like combinations, even though jets do not stem from a Z boson. The $M_{\ell\ell jj}$ distribution of these events is essentially a falling exponential above 220 GeV/c^2. Below that value, acceptance effects give rise to a steep edge difficult to reproduce with simulations.

To estimate the background from Z+jets and the shape of its $M_{\ell\ell jj}$ distribution, large exclusive simulated samples of Z + n jets ($n = 1$ to 4) events are used, corresponding to integrated luminosities ranging from 36 fb^{-1} to 232 fb^{-1} (appendix A). These samples have been thoroughly verified to reproduce the data in the m_{jj} sideband control region (for all observables but $M_{\ell\ell jj}$). The small discrepancies found are attributed to a bad modeling of the p_{T} spectrum of the $\ell^+\ell^- jj$ system, the so-called p_{T}^{H} observable.

While there are differences between data and simulations (Figure 10 (left)), the mismodeling of the p_{T} spectrum of the $\ell^+\ell^- jj$ system in the simulation is the same in the signal and sideband regions. A weight calculated as the ratio of the p_{T} distributions in data over simulations in the sideband region, and fitted to the function

$$f(p_{\mathrm{T}}) = \left(1 + \frac{1}{a + bp_{\mathrm{T}}^2}\right) \frac{1}{e^{-p_{\mathrm{T}}/c} + 1}$$

as function of p_{T} (Figure 10 (right)), is used to correct the Z+jets distributions in an event-by-event basis. To get a fair weight function, contamination from diboson events (obtained from

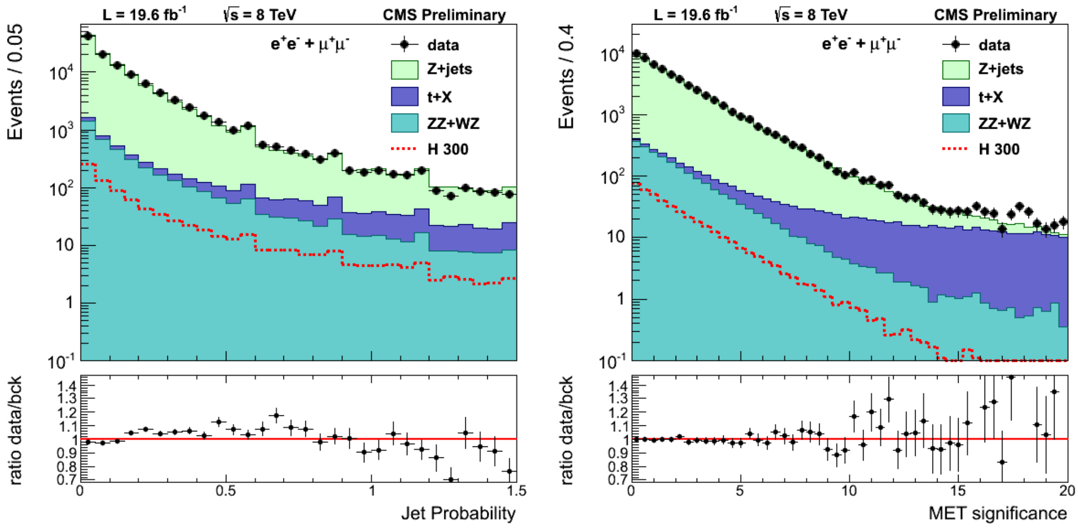

Figure 7: Left: jet probability b-tagger, after all selection cuts, for the three btag categories together. Right: corrected particle flow MET significance in data and simulation for events with electrons and muon combined, after the full selection except the cut on MET significance. The distributions of the background are normalized to data.

simulation) and $\mathrm{t\bar{t}}$ events (from data, see next section) is subtracted from data. Figure 11 depicts the fitted functions for different b-tag categories and their 1σ bands. The correction calculated with the inclusive sample, without distinguishing among b-tag categories, used in the analysis agrees within errors with the fit results obtained independently for each b-tag category.

In the final analysis, the Z+jets background is extracted from simulation, corrected using the p_{T} weight. Its normalization is constrained to the relative normalization of diboson+$\mathrm{t\bar{t}}$ background subtracted data in the m_{jj} sideband region, independently for each btag category.

Determination of $\mathrm{t\bar{t}}$ background from data

The $\mathrm{t\bar{t}}$ background is an important source of contamination in the 2-btag category. It is estimated from the data using $\mathrm{e}^{\pm}\mu^{\mp}$ events passing the same cuts as the signal. This method accounts for other small backgrounds (as WW + jets, $\mathrm{Z} \to \tau^+\tau^-$ + jets, single top, fakes) where the lepton flavor symmetry can be invoked as well.

In this study we use the Powheg + Pythia $\mathrm{t\bar{t}} \to 2\ell 2\nu + X$ Monte Carlo sample. Assuming a cross-section of 23.38 pb for this process, the top MC is normalized to the data for events with $M_{\mathrm{e}^{\pm}\mu^{\mp}} > 50\ \mathrm{GeV}/c^2$ using a K-factor of 1.06. Other top MC samples as the Madgraph $\mathrm{t\bar{t}}$ inclusive sample produce consistent results, but different K-factors are needed.

Top-pair Monte Carlo studies show that the $\mathrm{e}^{\pm}\mu^{\mp}$ vs. $\mathrm{e}^+\mathrm{e}^- + \mu^+\mu^-$ symmetry works very well at the level of the shapes of the distributions of all considered variables. Also, the relative event normalization is consistent with one, within the MC finite statistical errors. For instance, in the case of Powheg + Pythia top MC, the $\mathrm{e}^{\pm}\mu^{\mp}/(\mathrm{e}^+\mathrm{e}^- + \mu^+\mu^-)$ relative event normalizations are 1.007 ± 0.007 after selection and kinematical cuts, and 1.01 ± 0.01 after b-tagging.

Figure 12 shows a comparison of the $\mathrm{e}^+\mathrm{e}^- + \mu^+\mu^-$ and $\mathrm{e}^{\pm}\mu^{\mp}$ top MC distributions of two relevant variables, for events with at least two leptons and two jets passing selection cuts. More distributions are available in appendix G. The selection step is specified in each plot. In this studt the category "$\geq$ 1 b-tag" includes events with at least one jet tagged using the JPM

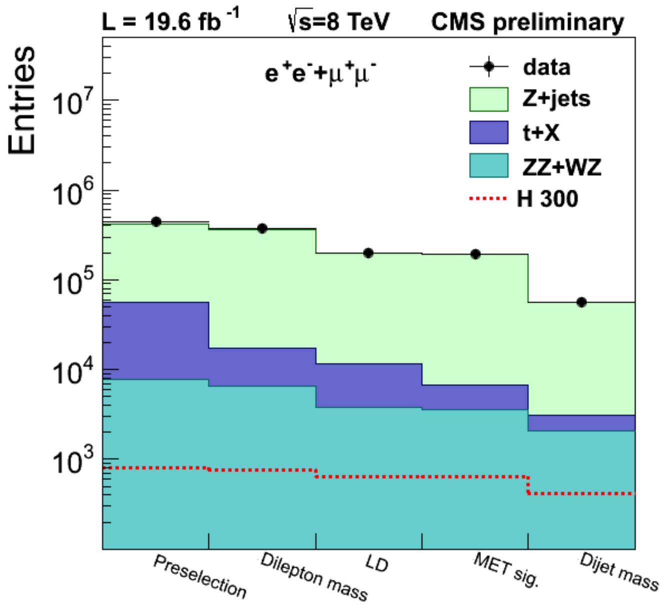

Figure 8: Numbers of events after each cut for the data, the background simulation, and a 300 GeV/c^2 Higgs boson signal.

prescription. The normalization is arbitrary.

Cuts	Top MC	Total MC	$e\mu$ data
$M_{ll} > 50$ GeV/c^2	26685.0	30238.6	30240
70 GeV/$c^2 < M_{ll} < 110$ GeV/c^2	9108.0	10403.8	10308
70 GeV/$c^2 < M_{jj} < 110$ GeV/c^2	1939.2	2261.4	2277
≥ 1 JPL b-tagged jet	1766.5	1941.6	1961
≥ 1 JPM b-tagged jet	1431.1	1545.1	1562
≥ 1 JPL & ≥ 1 JPM	873.7	922.4	950
1 JPL + 1 JPM, MET Sig < 10	357.5	381.9	406

Table 5: Comparison of 2012 $e\mu$ data to Powheg + Pythia top MC event yields, corresponding to an integrated luminosity of 19.6 fb^{-1}. "Total MC" contains the top, WW, $Z \rightarrow \tau^+\tau^-$, single top, and fakes contributions. Every cut in a line assumes all cuts in lines above.

The 2012 $e^\pm\mu^\mp$ data yields are compared to the sum of top MC prediction and other small backgrounds in Table 5, while distributions of relevant variables are shown in Figure 13 and appendix G. Events selected contain at least two leptons and two jets passing selection cuts. Only the hardest-$\sum P_T$ dilepton combination and the dijet combination with largest JP discriminator values are considered. Pile-up corrections have been applied. Other extra cuts are detailed where appropriate.

The table and figure above include an estimation of WW, $Z \rightarrow \tau^+\tau^-$, and single top contributions from Monte Carlo. The fake component is estimated from $e^\pm\mu^\mp$ data; the yield of events with one or two non-isolated leptons (in the combined relative isolation region 0.25 - 0.85), is extrapolated into the isolated lepton region assuming a flat distribution in the combined relative isolation variable. Changing the size of the non-isolation region changes the fake prediction by at most 10%. The e-μ symmetry holds in reasonable approximation for the non-isolated lepton data.

The sample composition before b-tagging is 86% $t\bar{t}$, 5% fakes, and 9% other small backgrounds. After requiring 1 JPL b-tag (1 JPM and 1 JPL b-tags) the relative fractions change to 91%(95%) $t\bar{t}$, 4%(2%) fakes, and 5%(3%) other small backgrounds.

Now, we test the $e^{\pm}\mu^{\mp}$ vs. $e^+e^- + \mu^+\mu^-$ symmetry using a top-enriched subsample of the data. Figure 14 (left) shows the MET significance distribution after requiring 1 JPM b-tag For values sufficiently large of MET significance the number of events of the $e^{\pm}\mu^{\mp}$ and $e^+e^- + \mu^+\mu^-$ samples are equal within statistical errors. In order to test the agreeement in shape, Figure 14 (right) contains the "Higgs" invariant mass distributions after requiring 2 (1 JPM + 1 JPL) btags, MET significance > 8, and $|M_{\ell^+\ell^-} - M_Z| > 20$ GeV/c^2. One can observe agreement on both the normalization and shape of the $e^{\pm}\mu^{\mp}$ and $e^+e^- + \mu^+\mu^-$ distributions. Appendix G has additional supporting figures for two btags (1 JPM and 1 JPL).

6 Systematics

In this section the systematic uncertainties affecting the analysis, the method used to estimate them and their calculated values are described.

Luminosity uncertainty

The latest recommendation for the 2012 datasamples is the uncertainty on LHC luminosity of 4.4% [29].

Higgs cross-section and branching fractions

The Higgs production cross-section uncertainty depends on production mechanism, either gluon fusion or weak boson fusion (WBF). However, since the gluon fusion mechanism dominates, it drives the total uncertainty. We use gg and WBF errors separately and for each mass point according to Yellow Report prescription. The total weighted error is in the range 13–15%.

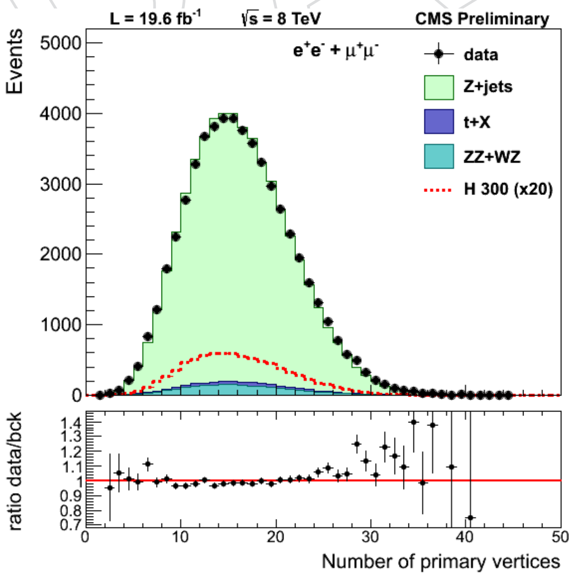

Figure 9: Reconstructed number of good vertices in data (points with error bars) and in reweighed simulation (solid histograms), from the electron and muon channels combined. The number of true interactions in MC has been reweighed to match the estimated distributions in data.

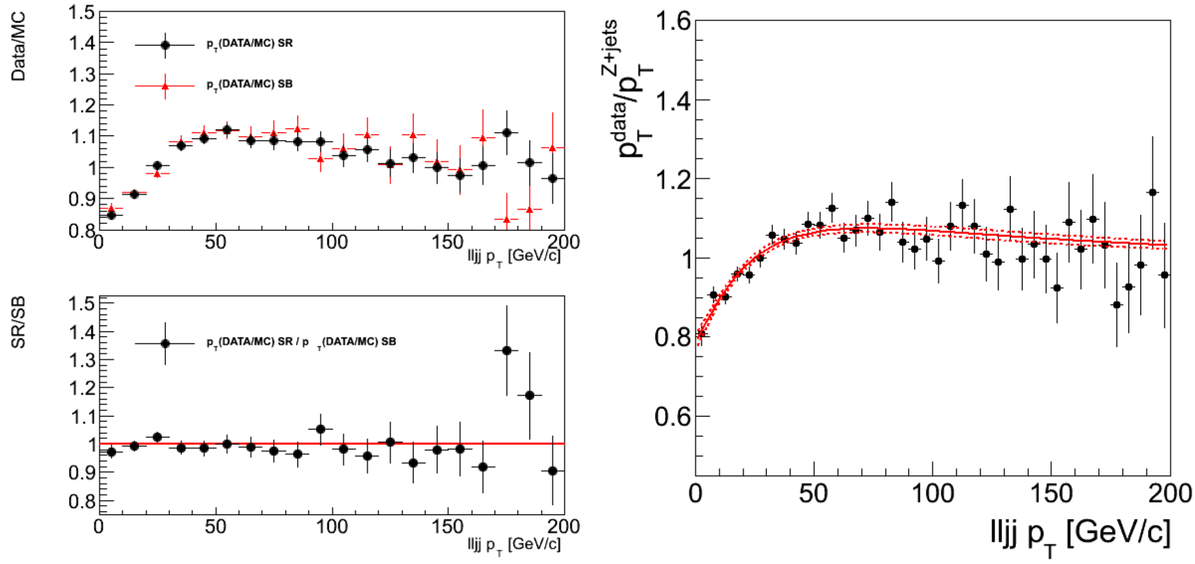

Figure 10: Left-top: data over Z+jets ratio of the p_{T} distributions of the $\ell^+\ell^- jj$ system in the m_{jj} sideband (red triangles) and signal (black dots) regions. Left-bottom: ratio of the ratios above. Right: ratio of the data over simulation p_{T} distributions together with the fit to $f(x)$ (red solid line). The red dashed lines are the $\pm 1\sigma$ statistical error bands calculated propagating the full correlation matrix of the fit.

We note that this uncertainty is relevant only for the measurement of the ratio to SM expectation R, while it does not affect the absolute cross-section measurement.

Uncertainties in the signal expectation

The main systematic uncertainties on signal normalization are summarized in Table 6, and are discussed in more detail in the subsection below.

Lepton trigger, identification and isolation

Lepton trigger, identification and isolation efficiencies are computed using the tag-and-probe technique; results are detailed in appendices B and C, respectively. For muons the total normalization uncertainty is 2.7%, with contributions from the trigger (2.5%), identification (1.0%), and isolation (0.4%). For electrons the total normalization uncertainty is 2%, dominated by identification (2%) and a much smaller contibution from the dielectron trigger efficiency.

Lepton energy scale

Normalization uncertainties related to the electron energy scale and the muon momentum scale are very small; always much below than 1%.

Jet Energy Scale and Resolution

The main uncertainty in jet reconstruction comes from jet energy scale (JES) uncertainty, while the uncertainty on the resolution contributes a much negligible effect to the total uncertainty. Our estimates show that JES variation by $\pm 1\sigma$ changes reconstruction efficiency of a 400 GeV/c^2 Higgs by about 1.2%. The effect on the jets transverse momentum and dijet invariant mass is sizable and it drives the bias on the acceptance. The change in selection efficiency as function of Higgs mass is summarized in table 7

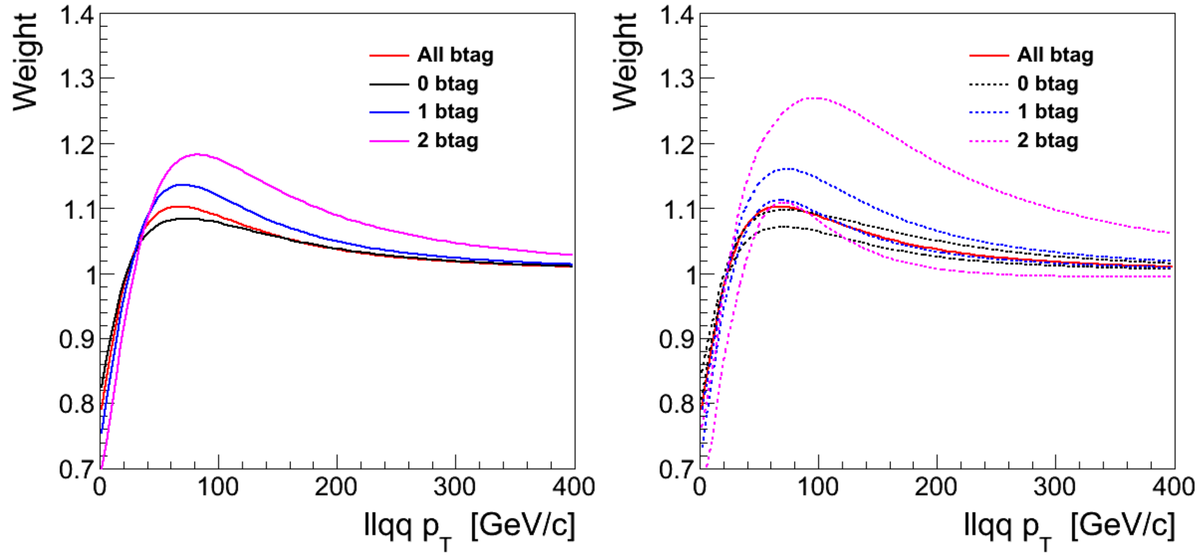

Figure 11: Fits to the ratios of the data over simulation p_T distributions of the $\ell^+\ell^- jj$ system in the different b-tag categories and their combination (left) and their corresponding 1σ bands (right).

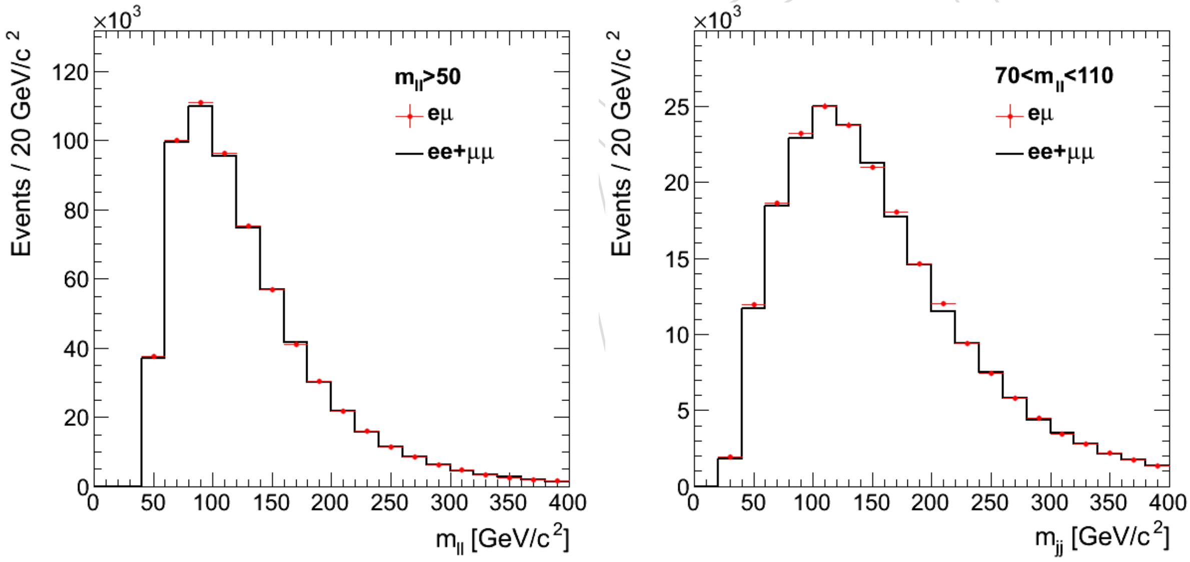

Figure 12: Powheg + Pythia top MC $e^\pm\mu^\mp$ to $(e^+e^- + \mu^+\mu^-)$ comparison for two variables after different steps of the selection, as specified in the legends: dilepton invariant mass (left) and dijet invariant mass (right).

Pileup

The number of true interactions per bunch crossing in the simulated samples was re-weighed to match the distributions in data. The main source of systematics may come from the uncertainty on the measurement of the amount of pileups in data. This uncertainty is studied by re-estimating the number of true interactions in data with different values of minimum-bias cross section as input, using 65.84 mb and 72.77 mb as recommended by the CMS pileup group [30], which is $\pm$5% difference with respect to the central value 69.30 mb. The re-estimated distributions and the central value are compared in Figure 15.

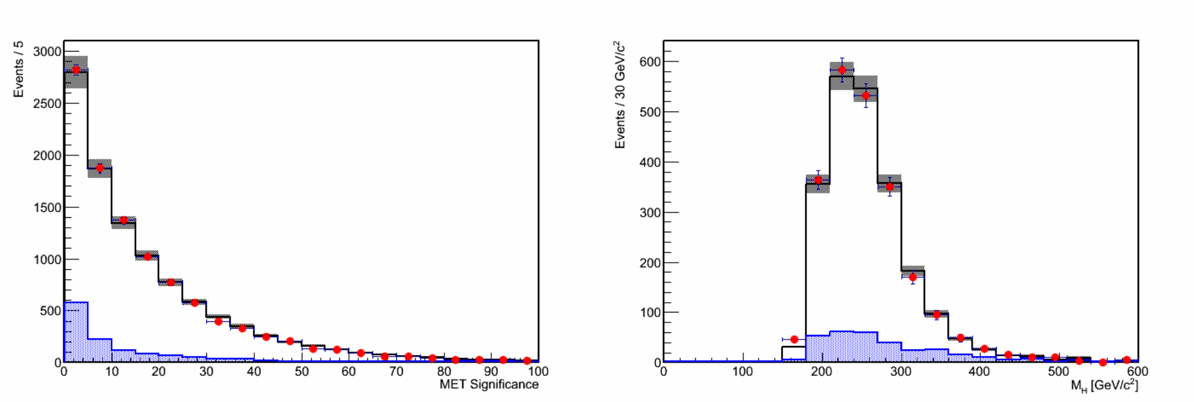

Figure 13: Comparison of 2012 $e^{\pm}\mu^{\mp}$ data to Powheg + Pythia top MC, corresponding to an integrated luminosity of 19.6 fb^{-1}. Red dots are $e^{\pm}\mu^{\mp}$ data; white histogram top Monte Carlo; blue histogram other small backgrounds. MET significance (left) and "Higgs" invariant mass (right).

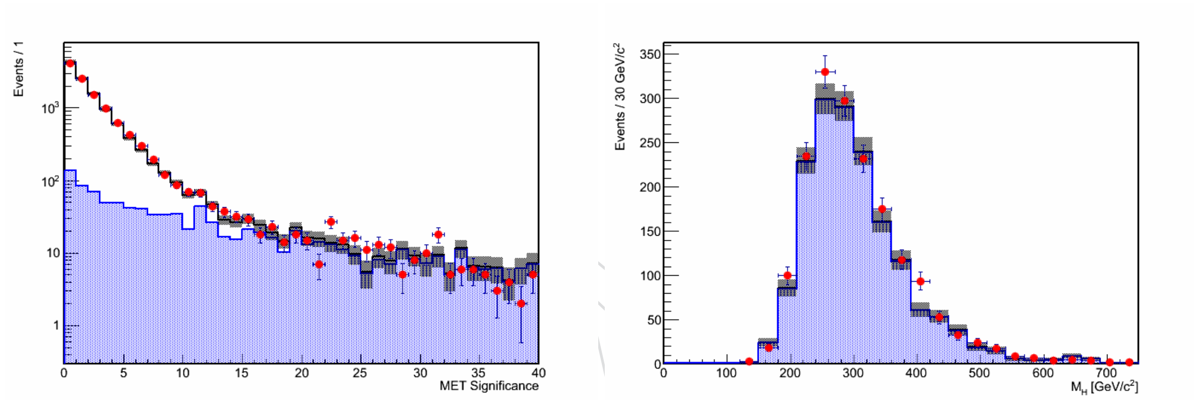

Figure 14: (Left) MET significance distribution for dilepton data compared to the sum of Drell-Yan Monte Carlo plus $e^{\pm}\mu^{\mp}$ data for events with 1 JPM b-tag. (Right) "Higgs" invariant mass (right) for $e^+e^- + \mu^+\mu^-$ and $e^{\pm}\mu^{\mp}$ data for events outside the leptonic Z mass window, with two (1 JPM + 1 JPL) b-tags, and MET significance > 8. Other cuts are detailed in the text. Red dots are $e^+e^- + \mu^+\mu^-$ data; white histogram Drell Yan Monte Carlo; blue histogram $e^{\pm}\mu^{\mp}$ data (plus other small backgrounds).

The number of true interactions are weighted in the MC to match the shifted distributions in data in Figure 15 and re-compute the signal efficiency. This leads to a change in the signal efficiency $< 1\%$ for the 0- and 1-btag categories, and about 2% for the 2-btag category, for $M_{\mathrm{H}} < 650$ GeV/c^2, approximately independent of lepton channel, as detailed in appendix H .

Heavy quark flavor tagging uncertainty

A data-to-Monte Carlo scale factor (SF_b) has been measured for events containing b-jets as a function of p_T and η for the jets. This SF_b corrects for the more efficient identification of b-jets in Monte Carlo compared to data. Likewise, a mistag rate scale factor (SF_{mistag}) for light quarks misreconstructed as b-jets has been measured over a range of p_T and η for the jets. To study the systematic effects of b-tagging, both the SF_b and SF_{mistag} were simultaneously varied up and down by the uncertainty related to each SF.

The study was performed separately for the muon and electron channels, calculating the effect for signal MC.

Tables in appendix H give the b-tagging systematic uncertainty for the signal, for muons and electrons. The systematic effect is computed in final regions moving the SF by plus and minus its uncertainty to the number of tagged jets with the nominal SF. The uncertainty is reported (in %) for the cases where both jets are tagged, at least 1 jet is tagged, and no jets are tagged. In the analysis, the exact systematic uncertainty as a function of the Higgs mass is applied.

MET uncertainty

The dominant effects are from the knowledge of the rest of the event, such as jet energy reconstruction and pileup. Therefore, both of the above subsections cover MET uncertainty to a large extent. Additionally we investigated how much the MET rescaling procedure described in section 4 affects the signal selection efficiency, by counting the number of signal events migrating over the MET threshold due to the scaling procedure. The requirement on the MET significance translates thus into about $\sim 0.5\%$ uncertainty on the final efficiency.

Production mechanism

The expected kinematics of the Higgs production is subject to uncertainties due to limited knowledge of the underlying parton distribution functions (PDFs) as well as the shortcomings in the theoretical prediction (missing higher orders in the perturbation series). These uncertainties are propagated to an uncertainty on the selection acceptance and efficiency. Their additional effect on the Higgs production cross section is discussed in a separate section below.

The PDF uncertainties is evaluated according to the PDF4LHC recommendations, by evaluating the selection efficiency for the PDF sets cteq66 [31], MSTW2008NLO [32] and NNPDF2.1 [33] and their error sets. The envelope of the various PDF sets is used as the total uncertainty, as recommended and amounts to 1-4%. The uncertainty noticeably increases for very high Higgs masses. A summary of systematic uncertainties on the signal acceptance following PDF4LHC recommendations can be found in table 8.

Additional uncertainties arise due to uncertainties on the Higgs signal shape that is theoretically calculated. The shape uncertainty is evaluated in the recommended way for the Higgs

Table 6: Summary of systematic uncertainties on signal normalization. Most sources are multiplicative errors on the cross-section measurement, except for expected Higgs cross-section (which is relevant for the measurement of the ratio to SM expectation R).

Source	0 b-tag	1 b-tag	2 b-tag	Comment
Muon trigger & ID	2.7%			Tag-&-probe study
Electron trigger & ID	2%			Tag-&-probe study
Electron energy scale	0.2%			
Muon momentum scale	0.1%			
Jet reconstruction	1-4%			JES, correlated among categories
b-tagging eff. and mistag rate	1-4%	1-5%	5-8%	Anti-correlated among categories
MET	$< 1\%$			Loose requirement
Pile-up	1-2%			Correlated between categories
Production mechanism (PDF)	1.5%			PDF4LHC, acceptance only
Production mechanism (lineshape)	0-3%			Only for $M_H > 400$ GeV/c^2
Luminosity	4.4%			Same for all analyses
Higgs cross-section (for R)	13-15%			Detailed table from YR available

decaying into a pair of Z boson, correctly accounting for the correct lineshape (i.e. reweighting of the given shape in POWHEG) which also accounts for interference effects. The full description of the reweighting and uncertainty method is given in [34] and provides an uncertainty that contributes in two ways: Due to the mass-dependence of the selection efficiency, the total signal effiency is affected by the line shape. The uncertainty is negligible below 400 GeV/c^2 and rises to $\sim 3\%$ at 600 GeV/c^2, with only small dependence on btag category.

Additionally the line-shape used in the CLs procedure is re-extracted with the alternative line-shape models (Figure 16 (left)). The tail caused by mismatched jets is not affected at all as it is a random mixture of events, averaging out any shifts from the uncertainty. The core of the signal distribution is only weakly affected byt the uncertainty. In the worst case (the highest mass we consider), the peak-position shifts by ~ 2 GeV/c^2 (compared to a sigma of 60 GeV/c^2) and the sigma changes by ~ 1 GeV/c^2. Due the minuscule effect of this uncertainty, it is not propagated further.

Background systematic uncertainties

We have evaluated the impact of the main systematic uncertainties on the background normalization and shape. The results are summarized in Table 9.

Lepton trigger and reconstruction uncertainties yield a 2% variation in the normalization of the $M_{\ell\ell jj}$ spectrum. Uncertainties on the muon momentum scale, electron energy scale, pile-up reweighting and the MET rescaling procedure described in section 4 have a negligible impact. Jet energy scale uncertainty causes an uncertainty on the normalization of 5.5%. The uncertainty on the scale factors for the b-tagging efficiency has an affect on the normalization of 0.4%, 0.8% and 4.5% for the the 0-, 1- and 2-btag categories respectively. The uncertainty on the b-tagging mistag rates introduces an uncertainty in the normalization of 1.9%, 7.8% and 6.2% for the the 0-, 1- and 2-btag categories respectively.

The impact on the $M_{\ell\ell jj}$ distributions of the uncertainties affecting the shape is displayed in Figures 17 and 18. Jet energy scale causes a $M_{\ell\ell jj}$-dependent uncertainty varying from almost 0 at low mass, up to 4% at 600 GeV/c^2.

To estimate the impact of the $p_T^{\ell\ell jj}$ correction described in section 5 we compare the $M_{\ell\ell jj}$ Z+jets background distributions with and without the correction. A mass-dependent systematic uncertainty is obtained as the difference of those distributions, and goes up to 3% at high $M_{\ell\ell jj}$ values.

Residual differences in the $M_{\ell\ell jj}$ distributions between the data and the background, in the M_{jj} sideband control region are taken as an additional mass-dependent systematic uncertainty. Those residual differences are plotted in Figure 19 (top). In order to smooth out the fluctuations, a linear variation as shown in the figure is used to incorporate this effect into alternative templates for the background prediction. The resulting alternative templates, around the nominal template, are shown in Figure 19 middle and bottom, for the electron and muon channels

Table 7: Signal efficiency changes due to systematic uncertainties on the jet energy scale.

M_H GeV/c^2	JES $+1\sigma$ (%)	JES -1σ(%)
230	4.3	-4.2
300	1.3	-1.3
400	1.2	-1.2
600	-0.8	0.9

respectively.

7 Statistical analysis and results

Signal determination

The signal efficiency of the selection described in section 4 is evaluated as the ratio between the number of selected events in each of the six channels (electron and muon channels, 0-, 1-, and 2-btag categories) under study and the total number of generated events in the Monte-Carlo samples. The signal efficiency as a function of the Higgs mass is fitted to a polinomium in order to be estimatated for those Higgs mass hypothesis where no Monte-Carlo sample is available, as shown in Figure 16 (right).

The narrow width approximation used in the 2011 analysis breaks down at high Higgs mass (typically > 400 GeV/c^2) due to the very large Higgs width (> 70 GeV/c^2). The problem has been discussed in details in Ref. [35] and a more correct approach to describe the Higgs invariant-mass distribution has been proposed, known as Complex Pole Scheme (CPS). The total Higgs production cross-section has been recomputed by the Higgs Cross-Section Working Group to include corrections due to CPS at high Higgs mass [36]. In the 2011 [3] and 2012 [37] published analysis, CPS effects were included in the cross section calculation, but neglected for the signal shape (covered by an appropriate uncertainty). In this analysis we properly reweight the simulated signal samples to follow the CPS.

At high Higgs mass the interference between the Higgs signal and the $gg \to ZZ$ background becomes large, as recently discussed in Ref. [38]. The effect of interference has been shown to be constructive below the Higgs mass peak and destructive above. It has therefore a negligible effect on the total cross-section (1-2%) but it biases the ZZ invariant-mass distribution. Moreover the interference has been computed only at LO while the signal is known at NNLO. In this analysis we follow the approach proposed in Ref. [38] to estimate the uncertainty due to missing higher perturbative order on the interference and the simulated line shape is reweighted accordingly.

After this is done, the obtained distribution after all the selection criteria should reflect the expectation for the Higgs events, both in yield and shape. This reweighting has been included in the analysis in order to account for the correct distributions.

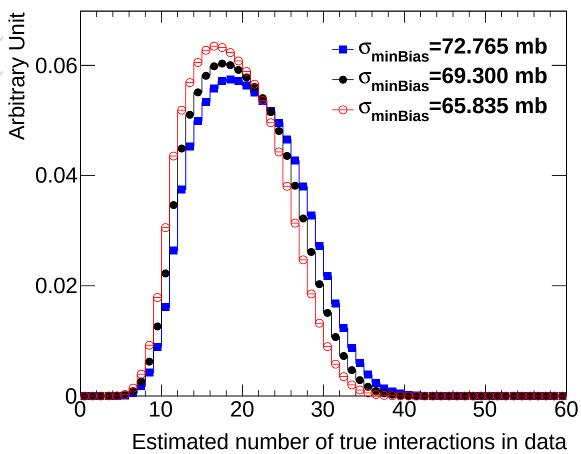

Figure 15: Estimated number of true interactions in 2012 data, assuming different values of minimum-bias cross section. The central value is 69.3 mb (solid circles).

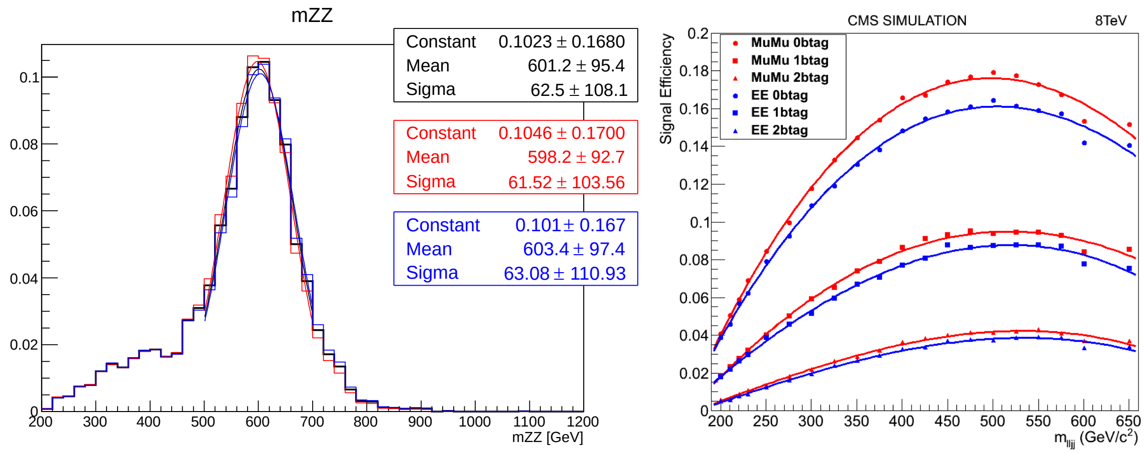

Figure 16: Left: reconstructed $M_{\mathrm{H}} = 600\,\mathrm{GeV}/c^2$ Higgs signal (area normalized) with the nominal lineshape (black) and systematic variations (blue/red). Gaussian fits to the core of the distribution are overlaid. Right: parameterization of the signal efficiencies, as function of the Higgs mass hypothesis, in the three btag categories, in the muon and electron channels.

Results

Since the decay products of the Higgs boson can be fully reconstructed, it is possible to use the reconstructed higgs boson mass, $M_{\ell\ell jj}$, distribution to discriminate Higgs signal events against background events. The reconstructed mass will peak around the true Higgs boson mass, M_{H}, for the signal, while for background processes it will have a broader distribution. Consequently, a shape-based treatment of the expected and observed distribution of the invariant mass of the Higgs candidate (i.e. the 4-object mass) increases the sensitivity of the analysis, compared to a simpler counting experiment. Since the expected shape of the background and the signal cannot be obtained from first principles, an analytical funcion cannot be used. Therefore, a binned histogram-based calculation has been used for the shape analysis.

The normalization of the simulated background (Z+jets and diboson) in the signal region is allowed to vary, the actual constraint coming from the number of events in the m_{jj} sideband. The signal-free regions of the $M_{\ell\ell jj}$ distribution in the signal region impose an additional constraint to the background normalization. The observed and expected numbers of events in the

Table 8: Systematic uncertainties on the signal acceptance following PDF4LHC recommendations.

	M_{H} (GeV/c^2)				
PDF	200	400	600	800	1000
CTEQ66	$^{+0.6}_{-0.7}$	$^{+0.8}_{-1.0}$	$^{+0.8}_{-1.1}$	$^{+1.5}_{-2.0}$	$^{+2.6}_{-3.2}$
MSTW2008NLO	$^{-0.2}_{-0.5}$	$^{+0.6}_{+0.2}$	$^{+0.8}_{+0.4}$	$^{+1.5}_{+0.7}$	$^{+2.5}_{+1.2}$
NNPDF2.1	$^{+0.8}_{+0.2}$	$^{+1.4}_{+0.75}$	$^{+1.5}_{+0.9}$	$^{+2.7}_{+1.4}$	$^{+4.3}_{-2.4}$
Total	$^{+0.8}_{-0.7}$	$^{+1.4}_{-0.8}$	$^{+1.5}_{-1.1}$	$^{+2.7}_{-2.0}$	$^{+4.3}_{-3.2}$

Table 9: Summary of systematic uncertainties on the normalization and shape of the background determination.

Source	Normalization	Shape
Muon trigger & ID	2.7%	
Muon momentum scale	0.1%	
Electron trigger & ID	2.0%	
Electron energy scale	0.5%	
Jet energy scale	5.5%	0-4%
b-tagging efficiency SF 0-tag	+0.4%	
b-tagging efficiency SF 1-tag	-0.8%	
b-tagging efficiency SF 2-tag	-4.5%	
Mistag SF 0-tag	-1.9%	
Mistag SF 1-tag	+7.8%	
Mistag SF 2-tag	+6.2%	
MET	0.3%	
Pile-up	0.1%	
$p_{\mathrm{T}}^{\ell\ell jj}$ weighting	0.8%	0-3%
Diboson cross section	15%	
Luminosity	4.4%	
Residual difference data-background in control region		0-15% (0-btag) 0-30% (1-btag) 0-40% (2-btag)

sideband region are given as input to the limit calculation tool. The calculation to discriminate signal from background events is performed independetly for the six individual analysis channels (electrons and muons in the 0, 1, and 2-btag categories), and then combined taking into account the correlations among the systematic uncertainties. These uncertainties may affect either the shape of the distributions or their normalization, and are properly taken into account in the statistical analysis.

The mass distributions of the $\ell^+\ell^- jj$ system are depicted in Figures 20 and 21 for data in the signal region. They include the systematic uncertainties on the background shape and normalization. The statistical uncertainty on the background is much smaller than the statistical uncertainty on the data, as the number of Z+jets simulated events used to estimate this background corresponds to a luminosity from 5 to 10 times larger. The full dataset (19.6 fb^{-1}) is used to assess the good modelling of the background in the m_{jj} sideband region (Figures 22 and 23). Residual differences are taken as a systematic uncertainty, as explained in section 6. As a cross check, we have studied the $M_{\ell\ell jj}$ distributions for the electron and muon channels separatelly, both in the m_{jj} sideband and signal regions (appendix I). They show an excellent agreement.

Expected upper limits on the SM Higgs boson production cross section are determined as function of the Higgs boson mass hypothesis, taking as input the $M_{\ell\ell jj}$ distribution for data, and for the background and signal expectations. The statistical procedure, based on the profile likelihood method, uses the *asymptotic CL_s* [39] approach, implemented in the official tool developed by the CMS Higgs combination group [40]. Systematic uncertainties are treated as nuisance parameters.

The results are expressed as upper limits on the ratio of the cross section times branching fraction of the process $\mathrm{H} \to \mathrm{ZZ} \to \ell^+\ell^- \mathrm{q\bar{q}}$ divided by the expectation for the standard model Higgs boson, $\sigma/\sigma_{\mathrm{SM}}$. A particular Higgs boson mass hypothesis is excluded whenever $\sigma/\sigma_{\mathrm{SM}} < 1$.

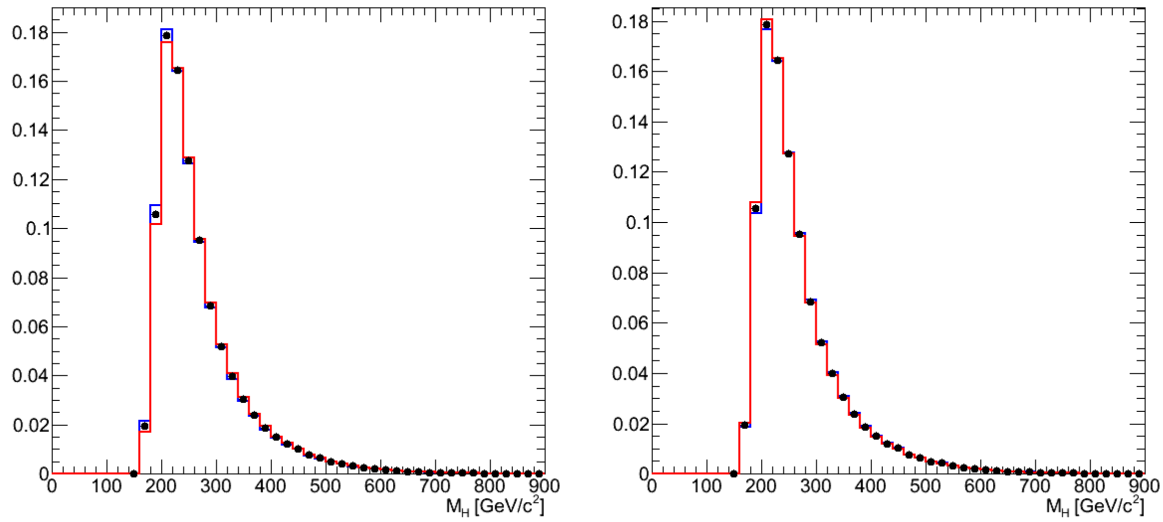

Figure 17: Shape variation of the $M_{\ell\ell jj}$ distribution for Z+jets simulated events when varying the systematic uncertainties: (left) jet energy scale, (right) $p_{\mathrm{T}}^{\ell\ell jj}$-based weigthing. Black dots denote the reference shapes. Red and blue histograms indicate the up and down variations of the corresponding systematic uncertainties.

The observed limit on $\sigma/\sigma_{\mathrm{SM}}$ is determined for M_{H} hypotheses between 230 GeV/c^2 and 650 GeV/c^2, using $M_{\ell\ell jj}$ distributions defined in the range from 220 GeV/c^2 to 800 GeV/c^2. The $M_{\ell\ell jj}$ region below 220 GeV/c^2 presents a very sharp rising edge difficult to have under control and is excluded from the analysis. Figure 24 shows the expected and observed limits (left) for the 5.3 fb^{-1} ICHEP data, and (right) for the full dataset recorded during 2012 at 8 TeV, corresponding to a luminosity of 19.6 fb^{-1}. With the increased luminosity in this dataset the 2-btag category becomes the most powerful contribution to the combination of the six channels (Figure 25). These results were cross-checked with an independent statistical method (appendix J). Other CMS searches have produced limits with on a much finer grid of resonance mass hypothesis. In order to combine our results with these searches, we interpolate the histograms used as for the signal hypothesis to those points where no simulation is available. For this interpolation we use the Radial-Basis-Function (RBF) method [41].

Limits on the SM production cross section times branching fraction for $\mathrm{H} \to \mathrm{ZZ}$ are presented in Figure 26. For comparison, expectations are shown for an SM-like Higgs boson.

In addition we combine the limits as observed in this study with the results of [3], as shown in Figure 27.

8 Conclusions

We have performed a search for a SM-like Higgs boson with a mass between 230 GeV/c^2 and 650 GeV/c^2 in the decay $\mathrm{H} \to \mathrm{ZZ} \to \ell^+\ell^- \mathrm{q\bar{q}}$, with the Z boson subsequently decaying to $\mathrm{Z} \to \ell^+\ell^-$ and $\mathrm{Z} \to \mathrm{q\bar{q}}$, using 19.6 fb^{-1} of data collected in summer 2012 from LHC proton-proton collisions at a centre-of-mass energy of 8 TeV. The analysis excludes the existence of a hypothetical standard-model-like Higgs boson in the mass range between 285 GeV/c^2 to 650 GeV/c^2, where the The expected exclusion range goes from 266 GeV/c^2 to 626 GeV/c^2.

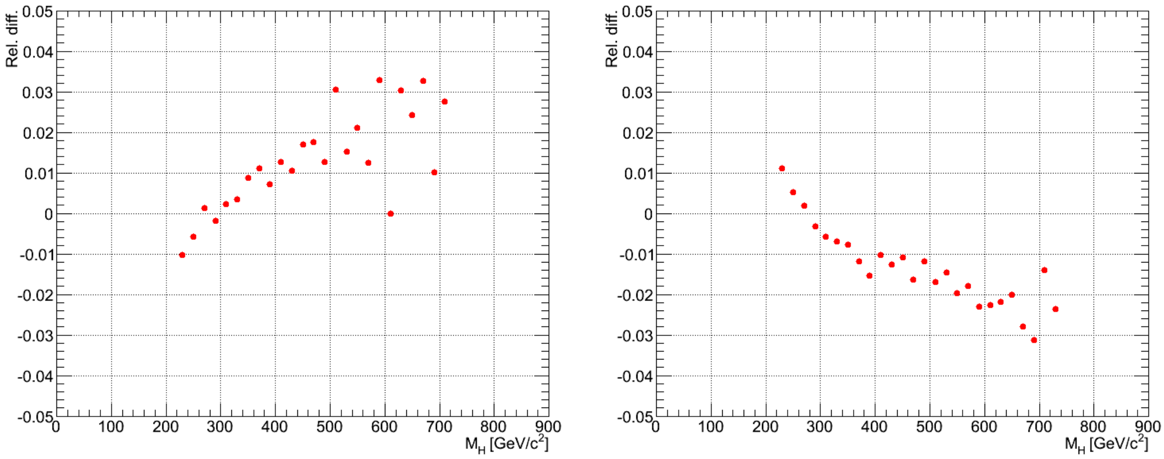

Figure 18: Relative difference on the shape of the $M_{\ell\ell jj}$ distribution for Z+jets simulated events when varying the systematic uncertainties: (left) jet energy scale, (right) $p_{\mathrm{T}}^{\ell\ell jj}$-based weigthing.

References

[1] CMS Collaboration, "Observation of a new boson at a mass of 125 GeV with the CMS experiment at the LHC", *Phys.Lett.* **B716** (2012) 30–61, `doi:10.1016/j.physletb.2012.08.021`, `arXiv:1207.7235`.

[2] ATLAS Collaboration, "Observation of a new particle in the search for the Standard Model Higgs boson with the ATLAS detector at the LHC", *Phys.Lett.* **B716** (2012) 1–29, `doi:10.1016/j.physletb.2012.08.020`, `arXiv:1207.7214`.

[3] CMS Collaboration, "Search for a Higgs boson in the decay channel $H \to ZZ(^{*}) \to q\bar{q}l^{-}l^{+}$", *JHEP* **04** (2012) 036, `doi:10.1007/JHEP04(2012)036`, `arXiv:1202.1416`.

[4] LHC Higgs Cross Section Working Group et al., "Handbook of LHC Higgs Cross Sections: 1. Inclusive Observables", *CERN-2011-002* (CERN, Geneva, 2011) `arXiv:1101.0593`.

[5] LHC Higgs Cross Section Working Group et al., "Handbook of LHC Higgs Cross Sections: 2. Differential Distributions", *CERN-2012-002* (CERN, Geneva, 2012) `arXiv:1201.3084`.

[6] Particle Data Group Collaboration, "Review of particle physics", *J. Phys.* **G37** (2010) 075021, `doi:10.1088/0954-3899/37/7A/075021`.

[7] S. Frixione, P. Nason, and C. Oleari, "Matching NLO QCD computations with Parton Shower simulations: the POWHEG method", *JHEP* **11** (2007) 070, `doi:10.1088/1126-6708/2007/11/070`, `arXiv:0709.2092`.

[8] The CMS generator group, "https://twiki.cern.ch/twiki/bin/viewauth/CMS/StandardModelCrossSectionsat8TeV", twiki, CERN, (2012).

[9] J. Alwall et al., "MadGraph/MadEvent v4: the new web generation", *JHEP* **09** (2007) 028, `doi:10.1088/1126-6708/2007/09/028`, `arXiv:0706.2334`.

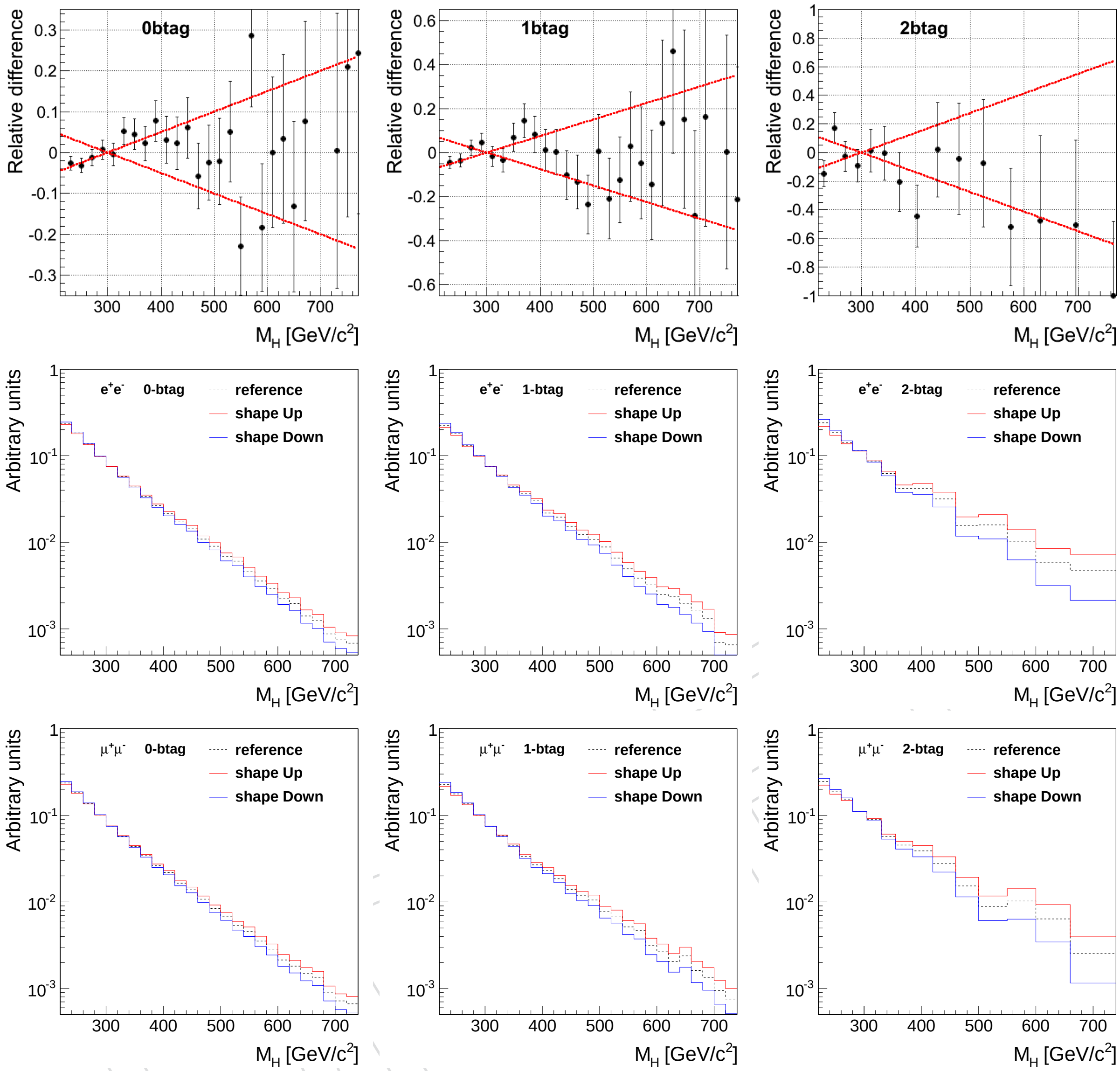

Figure 19: Residual differences in the $M_{\ell\ell jj}$ distributions between the data and the background, in the M_{jj} sideband control region (top). Alternative templates for the background prediction taking into account those residual variations, for the electron (middle) and the muon channels (bottom).

[10] T. Sjöstrand, S. Mrennan and P. Z. Skands, "PYTHIA 6.4 Physics and Manual", *JHEP* **05** (2006) 026, `doi:10.1088/1126-6708/2006/05/026`, `arXiv:hep-ph/0603175`.

[11] CMS, "https://twiki.cern.ch/twiki/bin/view/CMS/HiggsZZ2l2q2012Skims", twiki, CERN, (2012).

[12] CMS Collaboration Collaboration, "Performance of muon reconstruction and identification in pp collisions at $\sqrt{s}$=7 TeV", *CMS PAS* **CMS-MUO-10-004under approval** (2010).

[13] CMS Collaboration, "Performance of CMS muon identification in pp collisions at $\sqrt{s} = 7$ TeV", *CMS PAS* **MUO-2010-002** (2010).

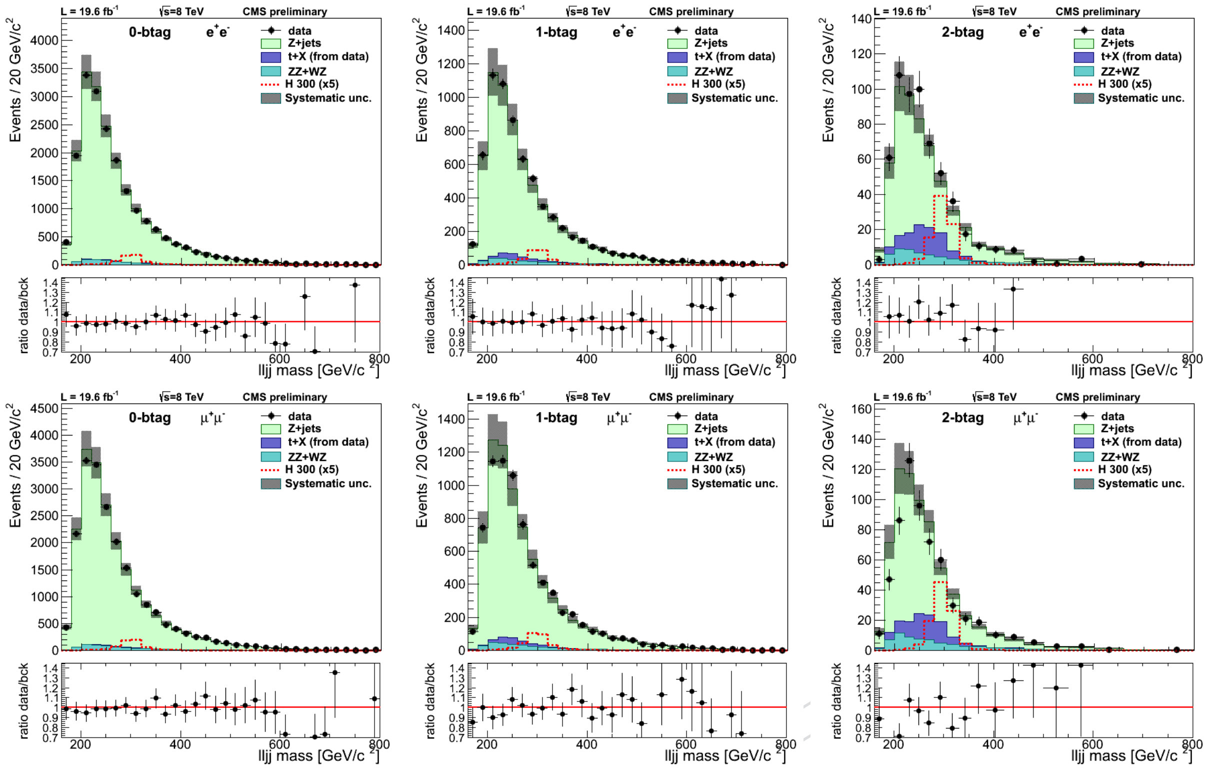

Figure 20: Mass distributions of the $\ell^+\ell^- jj$ system for events in the signal region in the electron (top) and muon (channels). From left to right, plots correspond to the 0-, 1-, and 2-btag categories. In the 2-btag category a variable bin size is used to compensate for the low number of events in the tail of the distributions. The dots are data, pale green histogram corrected Z+jets simulation, light blue simulated diboson background and dark blue $t\bar{t}$ events from data (which include single top, WW, $Z \to \tau^+\tau^-$+jets). The background is normalized to the data in the m_{jj} sideband. The grey band indicates the systematic uncertainty on the normalization and shape of the background, as estimated in section 6.

[14] CMS Collaboration, “Jet Performance in pp Collisions at $\sqrt{s}$=7 TeV”, CMS Physics Analysis Summary CMS-PAS-JME-10-003, CERN, (2010).

[15] CMS Collaboration, “Commissioning of the Particle-Flow Reconstruction in Minimum-Bias and Jet Events from pp Collisions at 7 TeV”, CMS Physics Analysis Summary CMS-PAS-PFT-10-002, CERN, (2010).

[16] CMS Collaboration, “Trigger strategies for Higgs searches in 2011”, CMS Analysis Note CMS-AN-2011-065, CERN, (2011).

[17] W. Adam et al., “Reconstruction of Electrons with the Gaussian-Sum Filter in the CMS Tracker at the LHC”, CMS Note 2005/001, CERN, (2005).

[18] CMS, “https://twiki.cern.ch/twiki/bin/view/CMS/EgammaCutBasedIdentification”, twiki, CERN, (2012).

[19] CMS, “https://twiki.cern.ch/twiki/bin/view/CMSPublic/SWGuideMuonId”, twiki, CERN, (2012).

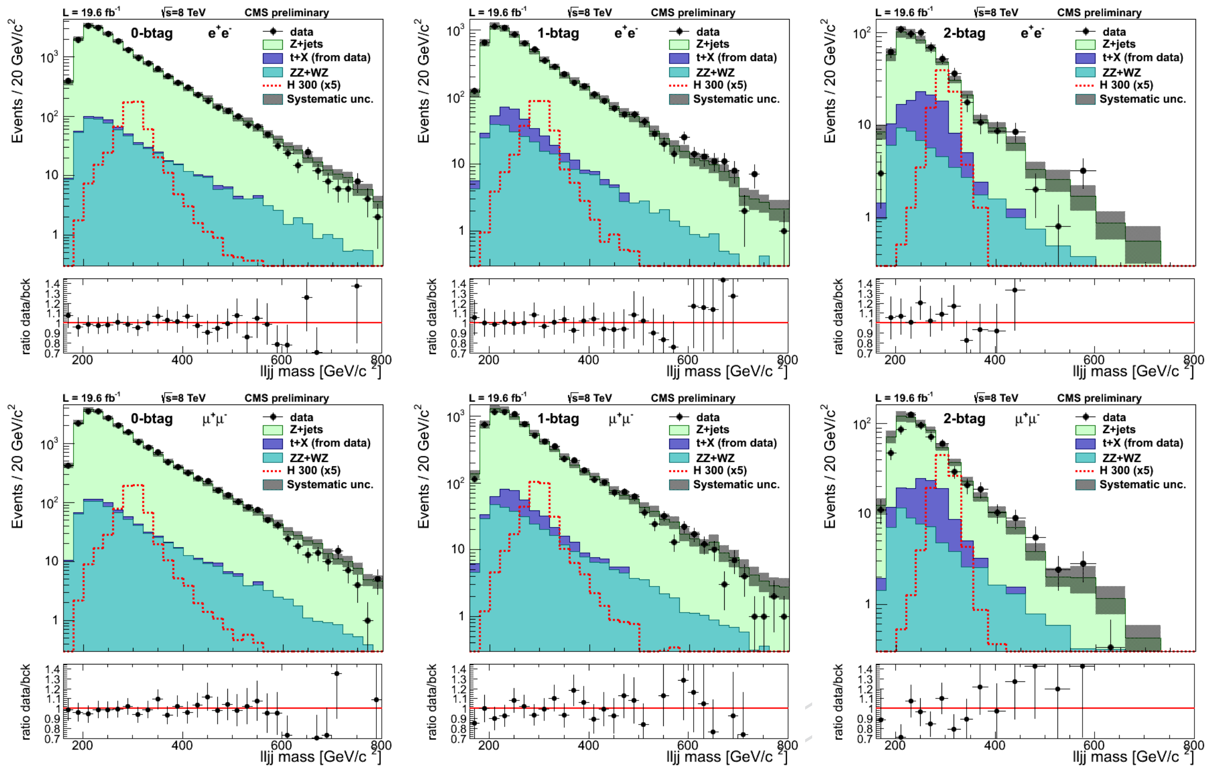

Figure 21: Mass distributions of Figure 20 in logarithmic scale.

[20] M. Cacciari, G. P. Salam, and G. Soyez, "The Anti-k(t) jet clustering algorithm", *JHEP* **0804** (2008) 063, `doi:10.1088/1126-6708/2008/04/063`, `arXiv:0802.1189`.

[21] CMS Collaboration, "Jet Energy Corrections determination at 7 TeV", CMS Physics Analysis Summary CMS-PAS-JME-10-010, CERN, (2010).

[22] M. Cacciari, G. P. Salam, and G. Soyez, "FastJet user manual (for version 3.0.2)", *Eur. Phys. J. C* **72** (2012) 1896, `doi:10.1140/epjc/s10052-012-1896-2`, `arXiv:1111.6097`.

[23] P. Van Hove and D. Bloch, "Mistag rate on b-tagging in 2012 data", CMS Note CMS-AN-2012/195, CERN, (2012).

[24] CMS Collaboration, "Identification of b-quark jets with the CMS experiment", `arXiv:1211.4462v1`.

[25] Y. Gao et al., "Spin determination of single-produced resonances at hadron colliders", *Phys.Rev.* **D81** (2010) 075022, `doi:10.1103/PhysRevD.81.075022`, `arXiv:1001.3396`.

[26] A. De Rujula et al., "Higgs look-alikes at the LHC", *Phys.Rev.* **D82** (2010) 013003, `doi:10.1103/PhysRevD.82.013003`, `arXiv:1001.5300`.

[27] CMS Collaboration, "Angular Analysis of Resonances $pp \to X \to ZZ$", CMS Analysis Note CMS-AN-2010-351, CERN, (2010).

[28] CMS Collaboration, "Missing transverse energy performance of the CMS detector", *JINST* **6** (2011) 09001, `doi:10.1088/1748-0221/6/09/P09001`.

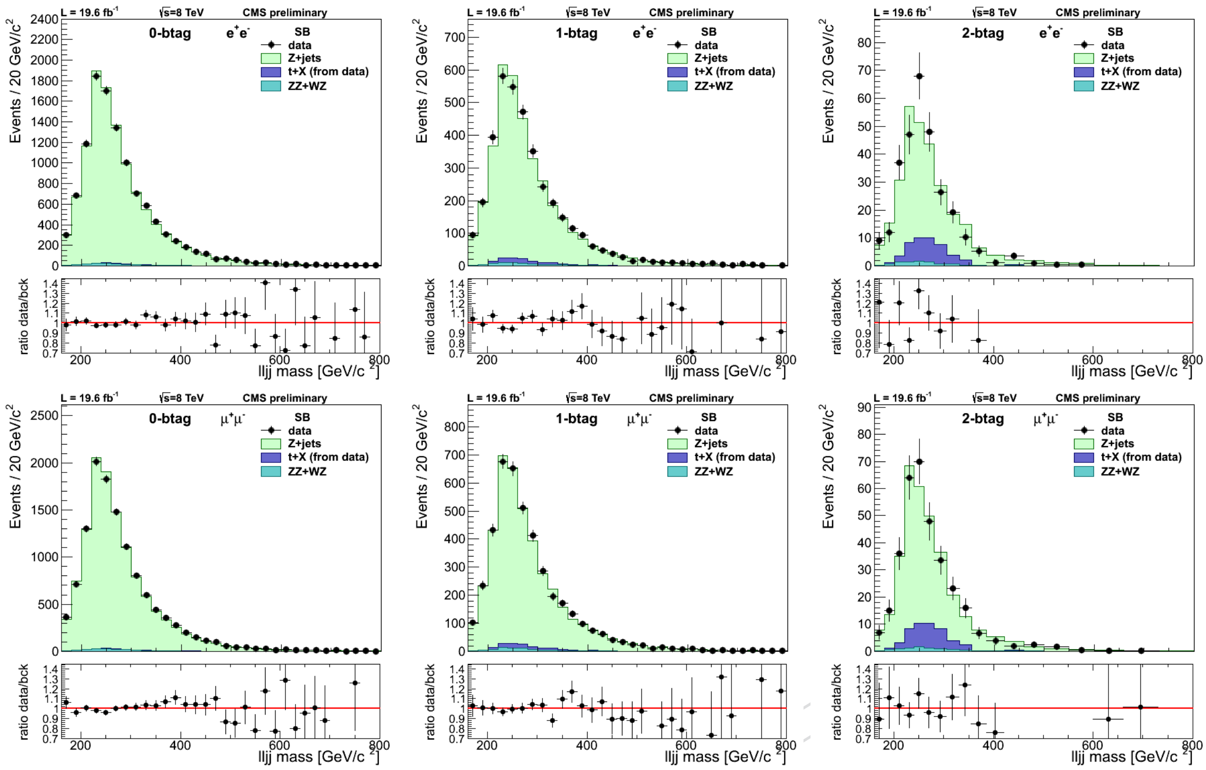

Figure 22: Mass distributions of the $\ell^+\ell^- jj$ system for events in the m_{jj} sideband region in the electron (top) and muon (channels). From left to right, plots correspond to the 0-, 1-, and 2-btag categories. In the 2-btag category a variable bin size is used to compensate for the low number of events in the tail of the distributions. The dots are data (19.6 fb^{-1}), pale green histogram corrected Z+jets simulation, light blue simulated diboson background and dark blue $t\bar{t}$ events from data (which include single top, WW, Z $\to \tau^+\tau^-$+jets).

[29] CMS Collaboration, “CMS Luminosity Based on Pixel Cluster Counting - Summer 2012 Update”, CMS Physics Analysis Summary CMS-PAS-LUM-12-001, CERN, (2012).

[30] Michael Hildreth, “Estimating Systematic Errors Due to Pileup Modeling”, twiki, CERN, (2012).

[31] P. M. Nadolsky et al., “Implications of CTEQ global analysis for collider observables”, *Phys.Rev.* **D78** (2008) 013004, `doi:10.1103/PhysRevD.78.013004`, `arXiv:0802.0007`.

[32] A. Martin et al., “Parton distributions for the LHC”, *Eur.Phys.J.* **C63** (2009) 189–285, `doi:10.1140/epjc/s10052-009-1072-5`, `arXiv:0901.0002`.

[33] R. D. Ball et al., “Impact of Heavy Quark Masses on Parton Distributions and LHC Phenomenology”, *Nucl.Phys.* **B849** (2011) 296–363, `doi:10.1016/j.nuclphysb.2011.03.021`, `arXiv:1101.1300`.

[34] CMS Collaboration, “Updated results on the new boson discovered in the search for the standard model Higgs boson in the H→ZZ→ 4ℓ channel in pp collisions at $\sqrt{s} = 7$ and 8 TeV”, CMS Analysis Note CMS-AN-2012-367, CERN, (2012).

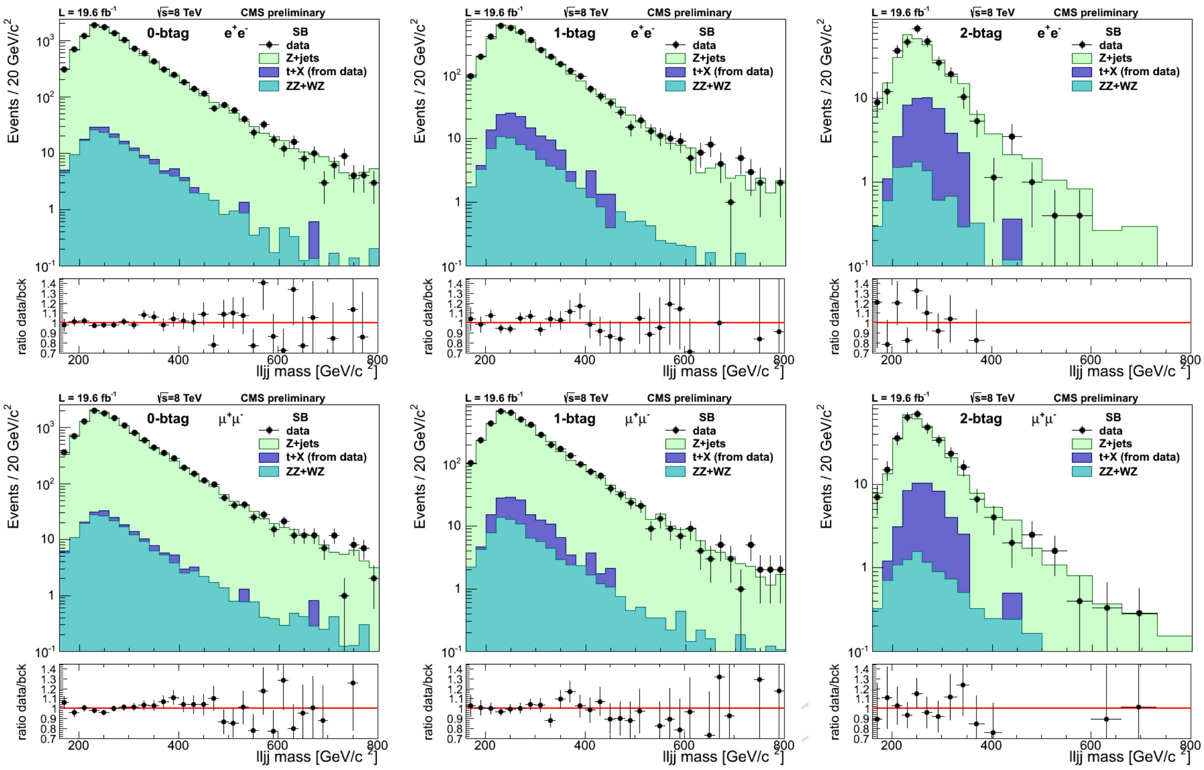

Figure 23: Mass distributions of Figure 22 in logarithmic scale.

[35] S. Goria, G. Passarino, and D. Rosco, "The Higgs Boson Lineshape", *Nucl.Phys.* **B864** (2012) 530–579, `doi:10.1016/j.nuclphysb.2012.07.006`, `arXiv:1112.5517`.

[36] CMS, "LHC Higgs Cross Section Working Group web page", https://twiki.cern.ch/twiki/bin/view/lhcphysics/, CERN, (2012).

[37] CMS Collaboration Collaboration, "Search for a standard-model-like Higgs boson with a mass of up to 1 TeV at the LHC", *Submitted to Eur. Phys. J. C* (2012) `arXiv:1304.0213v1`.

[38] G. Passarino, "Higgs Interference Effects in gg → ZZ and their Uncertainty", *JHEP* **1208** (2012) 146, `doi:10.1007/JHEP08(2012)146`, `arXiv:1206.3824`.

[39] G. Cowan, K. Cranmer, E. Gross, O. Vitells, "Asymptotic formulae for likelihood based tests of new physics", *Eur. Phys. J.* **C71** (2011) 1554, `arXiv:physics/1007.1727v2`.

[40] C. H. C. Group, "Documentation of the RooStats-based statistics tools for Higgs PAG", *CMS TWiki* `SWGuideHiggsAnalysisCombinedLimit` (2011).

[41] W. H. Press et al., "Numerical Recipes 3rd Edition: The Art of Scientific Computing",.

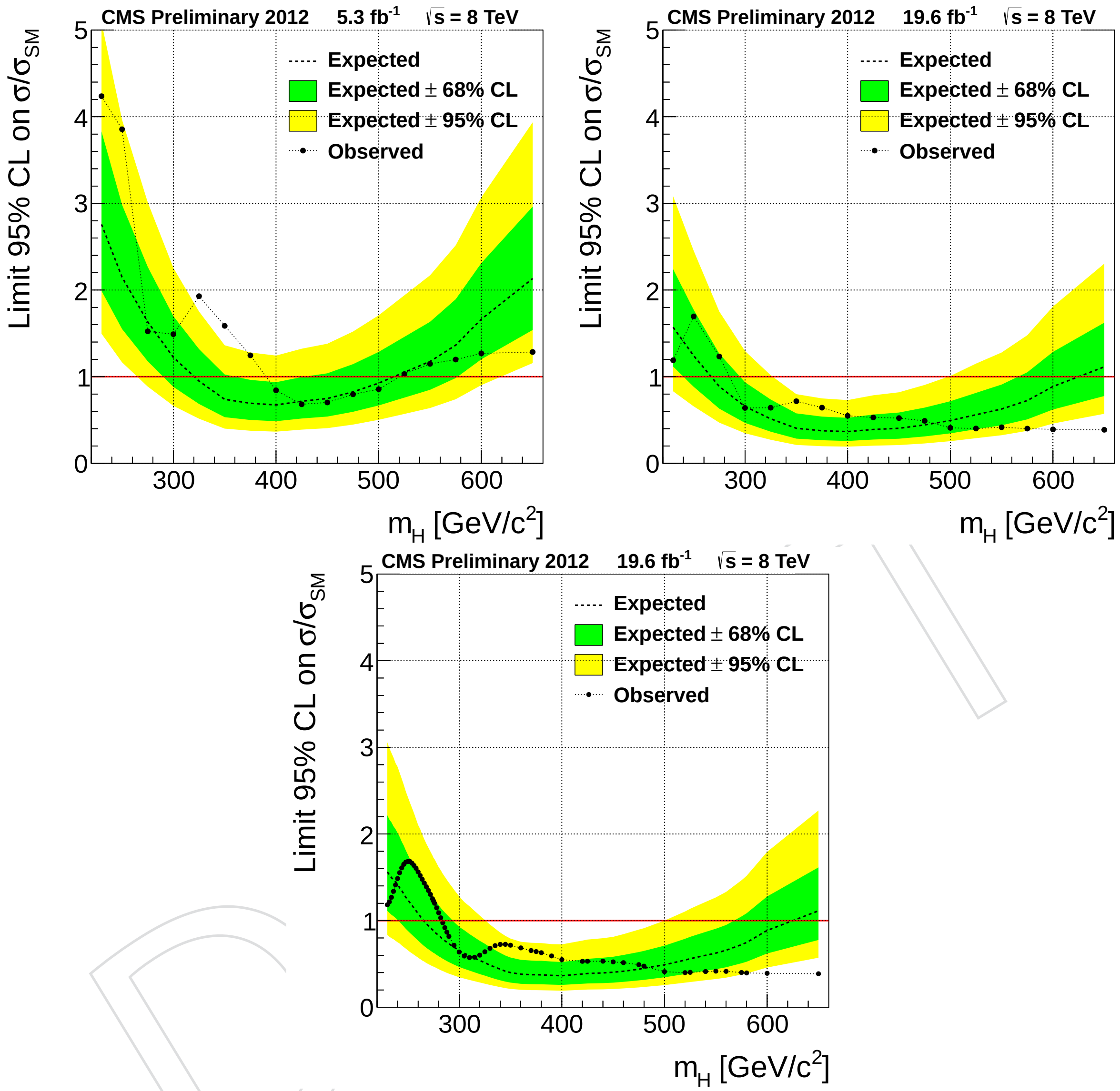

Figure 24: Observed (solid) and expected (dashed) 95% CL upper limit on the ratio of the production cross section to the SM expectation for the Higgs boson obtained using the CL_s technique. The 68% and 95% ranges of expectation for the background-only model are also shown with green and yellow bands, respectively. The solid line at 1 indicates the expectation for a SM-Higgs-like boson. The results on the top left correspond to a check performed on the unblinded part of the dataset (ICHEP data) to verify everything is under control. The plot on the top right shows the expected and observed limits using 19.6 fb^{-1} of data. The top plots show the observed limit only at the points where the signal shape can bedirectly obtained from the simulation. The bottom is equivalent to the top right plot, but additionally shows observed limit points where the signal shape has been obtained from interpolation for use in the CMS wide combination of results.

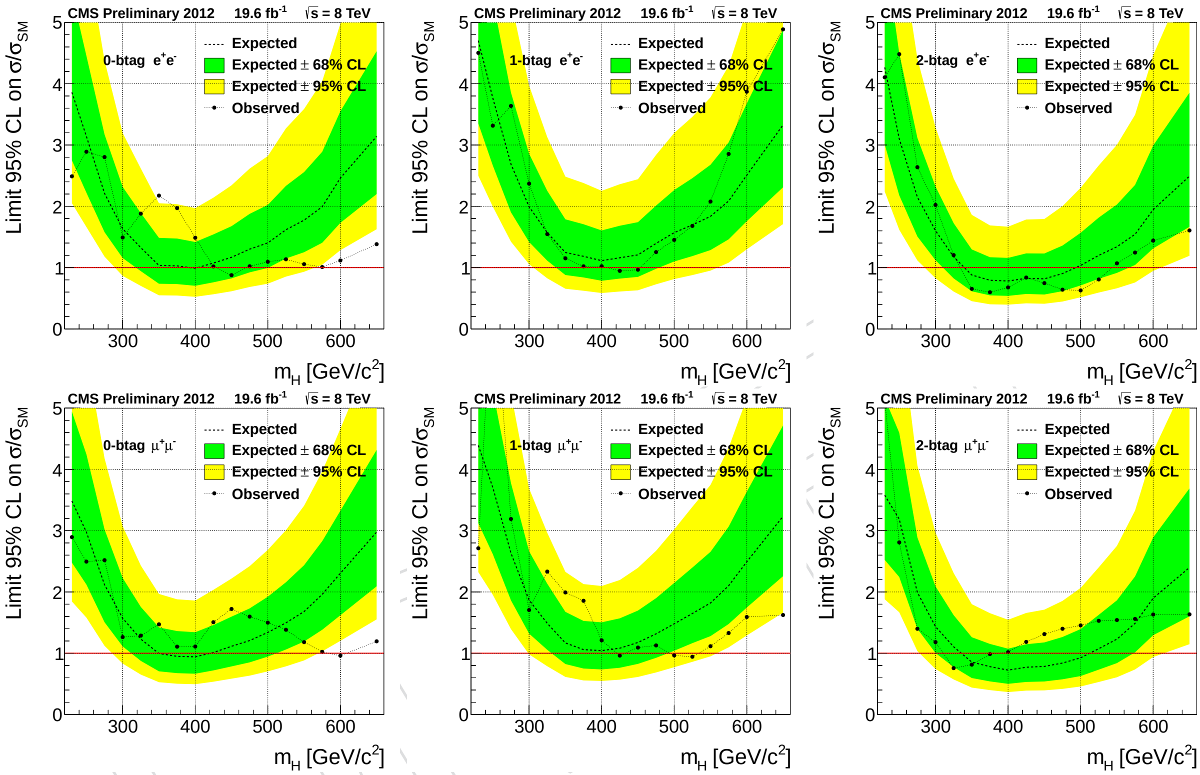

Figure 25: Observed (solid) and expected (dashed) 95% CL upper limit on the ratio of the production cross section to the SM expectation for the Higgs boson obtained using the CL_s technique, separate for the different lepton flavor and b-tag categories. The 68% and 95% ranges of expectation for the background-only model are also shown with green and yellow bands, respectively. The solid line at 1 indicates the expectation for a SM-Higgs-like boson.

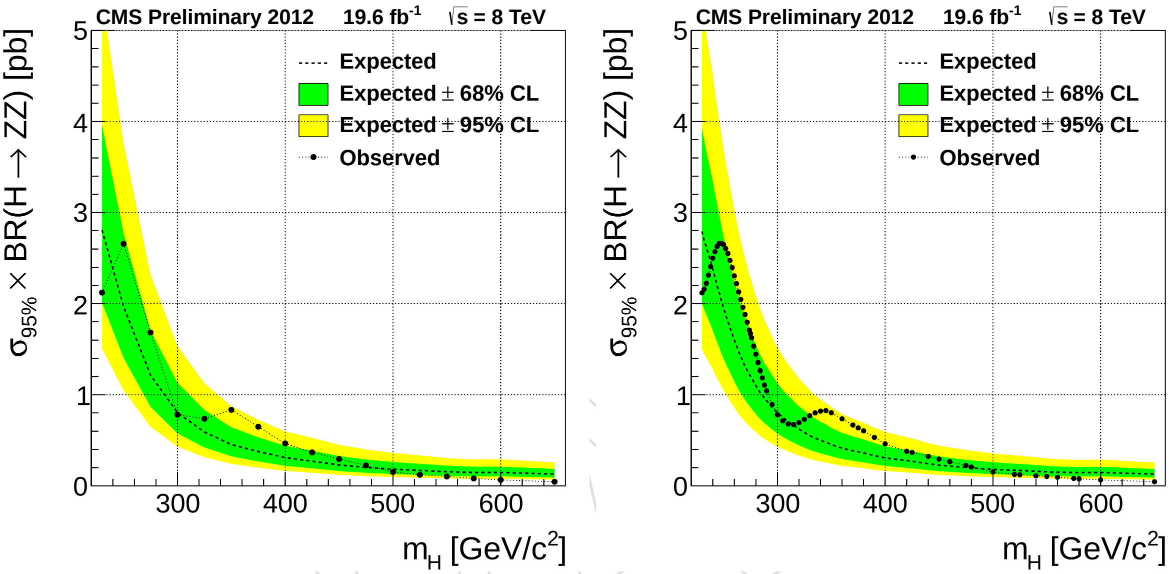

Figure 26: Observed (dashed) and expected (solid) 95% C.L. upper limit on the product of the production cross section and branching fraction for $H \rightarrow ZZ$ obtained with the CL_s technique. The 68% and 95% ranges of expectation for the background-only model are also shown with green and yellow bands, respectively. The left plot shows the observed limit only at the points where the signal shape can bedirectly obtained from the simulation. The right plot additionally shows observed limit points where the signal shape has been obtained from interpolation for use in the CMS wide combination of results.

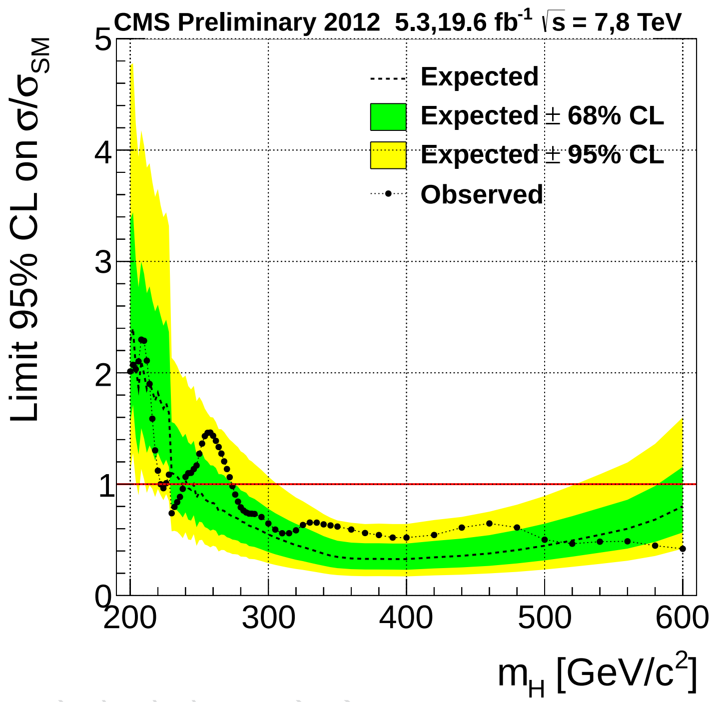

Figure 27: Observed (solid) and expected (dashed) 95% CL upper limit on the ratio of the production cross section to the SM expectation for the Higgs boson obtained using the CL_s technique. The 68% and 95% ranges of expectation for the background-only model are also shown with green and yellow bands, respectively. The solid line at 1 indicates the expectation for a SM-Higgs-like boson. This result is the combination of this study (i.e. Figure 24) with previous results.

A Data and Monte Carlo samples

Table 10 lists the data samples used in the analysis and their corresponding luminosities. The signal samples and their cross-section times branchig-ratio values are reported in Table 11. Table 12 provides the background datasets, along with their cross sections and luminosities.

Table 10: Data samples used in the analysis.

Channel	Dataset	Luminosity [pb^{-1}]
$2\mu 2q$	/DoubleMu/Run2012A-13Jul2012-v1/AOD	808
	/DoubleMu/Run2012A-recover-06Aug2012-v1/AOD	82
	/DoubleMu/Run2012B-13Jul2012-v4/AOD	4429
	/DoubleMu/Run2012C-24Aug2012-v1/AOD	495
	/DoubleMu/Run2012C-EcalRecover_11Dec2012-v1/AOD	134
	/DoubleMu/Run2012C-PromptReco-v2/AOD	6394
	/DoubleMu/Run2012D-PromptReco-v1/AOD	7274
$2e2q$	/DoubleElectron/Run2012A-13Jul2012-v1/AOD	808
	/DoubleElectron/Run2012A-recover-06Aug2012-v1/AOD	82
	/DoubleElectron/Run2012B-13Jul2012-v4/AOD	4429
	/DoubleElectron/Run2012C-24Aug2012-v1/AOD	495
	/DoubleElectron/Run2012C-EcalRecover_11Dec2012-v1/AOD	134
	/DoubleElectron/Run2012C-PromptReco-v2/AOD	6394
	/DoubleElectron/Run2012D-PromptReco-v1/AOD	7274
$e\mu qq$	/MuEG/Run2012A-13Jul2012-v1/AOD	808
	/MuEG/Run2012A-recover-06Aug2012-v1/AOD	82
	/MuEG/Run2012B-13Jul2012-v4/AOD	4429
	/MuEG/Run2012C-24Aug2012-v1/AOD	495
	/MuEG/Run2012C-EcalRecover_11Dec2012-v1/AOD	134
	/MuEG/Run2012C-PromptReco-v2/AOD	6394
	/MuEG/Run2012D-PromptReco-v1/AOD	7274

Table 11: The signal samples, $H \to ZZ \to \ell^+\ell^-\,q\bar{q}$ ($\ell = e, \mu, \tau$), simulated with POWHEG are */GluGluToHToZZTo2L2Q_M-xyz_8TeV-powheg-pythia6/Summer12_DR53X-PU_S10_START53_V7A-v1/AODSIM* , where *xyz* is the Higgs boson mass hypothesis, M_H. The cross section times branching fraction for each M_H value is listed in pb.

M_H (GeV/c^2)	$\sigma\times$ Br($H \to ZZ \to \ell^+\ell^-\,q\bar{q}$) [pb]	M_H (GeV/c^2)	$\sigma\times$ Br($H \to ZZ \to \ell^+\ell^-\,q\bar{q}$) [pb]
200	0.2566	400	0.1111
210	0.2538	425	0.0914
220	0.2416	450	0.7311
230	0.2278	475	0.6000
250	0.2022	500	0.4719
275	0.1751	525	0.0380
300	0.1563	550	0.0305
325	0.1478	575	0.0250
350	0.1482	600	0.0201
375	0.1360		

Table 12: Background simulated samples of the Summer12 production used in the analysis. The equivalent luminosity of the processed events for each sample is computed using the (N)NLO cross section in the 3rd column.

Process	dataset	σ [pb]	luminosity [fb^{-1}]
Z+jets (inclusive)	/DYJetsToLL_M-50_TuneZ2Star_8TeV-madgraph-tarball/ Summer12_DR53X-PU_S10_START53_V7A-v1/AODSIM	3503.71	8.7
Z+1 jet (exclusive)	/DY1JetsToLL_M-50_TuneZ2Star_8TeV-madgraph/ Summer12_DR53X-PU_S10_START53_V7A-v1/AODSIM	660.6	36.4
Z+2 jet (exclusive)	/DY2JetsToLL_M-50_TuneZ2Star_8TeV-madgraph/ Summer12_DR53X-PU_S10_START53_V7A-v1/AODSIM	215.1	101.6
Z+3 jet (exclusive)	/DY3JetsToLL_M-50_TuneZ2Star_8TeV-madgraph/ Summer12_DR53X-PU_S10_START53_V7A-v1/AODSIM	65.79	167.4
Z+4 jet (exclusive)	/DY4JetsToLL_M-50_TuneZ2Star_8TeV-madgraph/ Summer12_DR53X-PU_S10_START53_V7A-v1/AODSIM	27.59	232.1
$t\bar{t}$	/TTTo2L2Nu2B_8TeV-powheg-pythia6/ Summer12_DR53X-PU_S10_START53_V7A-v1/AODSIM	23.38	461
ZZ	/ZZ_TuneZ2star_8TeV_pythia6_tauola/ Summer12_DR53X-PU_S10_START53_V7A-v1/AODSIM	17.654	549
WZ	/WZ_TuneZ2star_8TeV_pythia6_tauola/ Summer12_DR53X-PU_S10_START53_V7A-v1/AODSIM	22.88	424
WW	/WW_TuneZ2star_8TeV_pythia6_tauola/ Summer12_DR53X-PU_S10_START53_V7A-v1/AODSIM	57.1097	168

B Trigger efficiencies and Monte Carlo correction factors

The trigger efficiencies and MC correction factors used in the analysis are listed in Tables 13 and 14 for the electron triggers, and in Table 15 for the muon trigger.

Table 13: Working point loose to the HLT Ele8 leg tag-and-probe efficiencies and scale factors.

η coverage	p_T range (GeV/c)	efficiency (data)	efficiency (MC)	data/MC ratio
$0.0 < \|\eta\| < 0.8$	$20 < p_T < 40$	0.986 ± 0.001	0.988 ± 0.001	0.997 ± 0.001
$0.8 < \|\eta\| < 1.4$		0.936 ± 0.001	0.946 ± 0.001	0.990 ± 0.002
$1.6 < \|\eta\| < 2.0$		0.901 ± 0.002	0.905 ± 0.003	0.995 ± 0.004
$2.0 < \|\eta\| < 2.5$		0.944 ± 0.002	0.944 ± 0.002	1.000 ± 0.003
$0.0 < \|\eta\| < 0.8$	$40 < p_T < 200$	0.991 ± 0.001	0.994 ± 0.001	0.997 ± 0.000
$0.8 < \|\eta\| < 1.4$		0.976 ± 0.001	0.978 ± 0.001	0.998 ± 0.001
$1.6 < \|\eta\| < 2.0$		0.945 ± 0.002	0.946 ± 0.002	0.999 ± 0.002
$2.0 < \|\eta\| < 2.5$		0.962 ± 0.002	0.962 ± 0.002	1.000 ± 0.002

Table 14: Working point loose to the HLT Ele17 leg tag-and-probe efficiencies and scale factors.

η coverage	p_T range (GeV/c)	efficiency (data)	efficiency (MC)	data/MC ratio
$0.0 < \|\eta\| < 0.8$	$20 < p_T < 40$	0.983 ± 0.001	0.984 ± 0.001	0.999 ± 0.001
$0.8 < \|\eta\| < 1.4$		0.932 ± 0.001	0.940 ± 0.001	0.991 ± 0.002
$1.6 < \|\eta\| < 2.0$		0.895 ± 0.002	0.898 ± 0.003	0.997 ± 0.004
$2.0 < \|\eta\| < 2.5$		0.933 ± 0.002	0.935 ± 0.003	0.998 ± 0.003
$0.0 < \|\eta\| < 0.8$	$40 < p_T < 200$	0.989 ± 0.001	0.991 ± 0.001	0.998 ± 0.001
$0.8 < \|\eta\| < 1.4$		0.972 ± 0.001	0.973 ± 0.001	0.999 ± 0.001
$1.6 < \|\eta\| < 2.0$		0.938 ± 0.002	0.939 ± 0.002	0.999 ± 0.002
$2.0 < \|\eta\| < 2.5$		0.951 ± 0.002	0.955 ± 0.002	0.996 ± 0.003

Table 15: Dimuon trigger efficiencies, calculated using the Muon POG official numbers, for two tight muons, both with $p_{\mathrm{T}} > 20$ GeV/c, in four bins of pseudorapidity for each of the two muons.

muon η	$0.0 < \|\eta\| < 0.9$	$0.9 < \|\eta\| < 1.2$	$1.2 < \|\eta\| < 2.1$	$2.1 < \|\eta\| < 2.4$
$0.0 < \|\eta\| < 0.9$	0.938 ± 0.011	0.880 ± 0.014	0.864 ± 0.012	0.880 ± 0.021
$0.9 < \|\eta\| < 1.2$	0.880 ± 0.014	0.836 ± 0.021	0.824 ± 0.017	0.819 ± 0.047
$1.2 < \|\eta\| < 2.1$	0.864 ± 0.012	0.824 ± 0.017	0.813 ± 0.010	0.804 ± 0.021
$2.1 < \|\eta\| < 2.4$	0.880 ± 0.021	0.819 ± 0.047	0.804 ± 0.021	0.784 ± 0.063

As a cross check, we have compared the trigger efficiencies calculated from data with the trigger efficiencies provided by the HLT trigger simulation. Table 16 shows the trigger simulation efficiencies for the Z+jets and Higss signal (300 GeV/c^2) simulated samples. The ratio between the trigger efficiencies calculated from data and the trigger simulation, averaged over η, is 0.94, both for the Z+jets and Higss signal (300 GeV/c^2) simulated samples. This discrepancy can be explained by the missing cut on the longitudinal distance between the two muons (Δz) in the muon trigger simulation. The Muon POG is recalculating the data/MC trigger efficiency scale factors to take this effect into account. It is important to note that we are applying to the MC the trigger efficiencies calculated from data, listed in table 15, hence this effect is taken into account. In any case, this small discrepancy would only be relevant for the signal, given the background normalization is constrained to the data in the m_{jj} sideband region.

We have performed the same study for electrons. The overall trigger effiencies calculated from data and from the trigger simulation, averaged over p_{T} and η, agree within 1%.

Table 16: Muon trigger efficiencies from trigger simulation for the Z+jets and Higss signal (300 GeV/c^2) simulated samples.

	Z+jets				Higgs signal, 300 GeV/c^2			
muon η	$0-0.9$	$0.9-1.2$	$1.2-2.1$	$2.1-2.4$	$0-0.9$	$0.9-1.2$	$1.2-2.1$	$2.1-2.4$
$0-0.9$	0.97	0.94	0.93	0.92	0.97	0.94	0.94	0.93
$0.9-1.2$	0.94	0.91	0.91	0.89	0.94	0.91	0.90	0.91
$1.2-2.1$	0.93	0.91	0.90	0.88	0.93	0.91	0.91	0.88
$2.1-2.4$	0.92	0.88	0.88	0.85	0.90	0.89	0.88	0.97

C Lepton identification requirements and efficiencies

The standard tag-&-probe method used to evaluate the lepton identification efficiencies from data requires the reconstruction of the dilepton system with invariant mass in the range [60-120] GeV/c^2. One of the leptons, called tag, is required to pass full selection criteria and to match the tighter leg of the trigger. The other lepton candidate, called probem is selected with criteria that depend on the efficiency being measured. The sample is divided into two exclusive subsamples depending on whether the probe lepton passes or fails the selection criteria currently under investigation. Due to the presence of background events, the signal yields are obtained with a fit to the invariant mass distribution of the dilepton system. The measured efficiency is calculated as a function of p_T and η of the probe lepton from the relative yields of the signal in subsamples with passing or failing probes. Finally the data to MC scale factors are deduced by dividing the efficiencies in data to the ones obtained from MC using exactly same procedure. Scale factors are used instead of raw efficiencies in order to benefit from partial cancellations of systematic uncertainites associated with the procedure. The total efficiency measurement is factorized into five sequential relative efficiency measurements: tracking, reconstruction, identification, isolation and the total trigger efficiency, given by the product:

$$\epsilon_{lepton} = \epsilon_{tracking} \times \epsilon_{RECO/Tracking} \times \epsilon_{ID/RECO} \times \epsilon_{ISO/ID} \times \epsilon_{Trigger/ISO}$$

Lepton identification requirements are given in Table 17 for electrons, and in Table 18 for muons. The data to simulation scale factors for these electron and muon identification requirements are listed in Table 19.

Table 17: Electron ID requirements for the Loose ID working point.

Variable	Barrel cut	Endcap cut
$\Delta\eta_{trk,supercluster}$	< 0.007	< 0.009
$\Delta\phi_{trk,supercluster}$	< 0.15	< 0.1
$\sigma_{i\eta,i\eta}$	< 0.01	< 0.03
H/E	< 0.12	< 0.10
d_0 (wrt primary vertex)	< 0.2 mm	< 0.2 mm
d_z (wrt primary vertex)	< 2 mm	< 2 mm
$\|1/E - 1/p\|$	< 0.05	< 0.05
$I_{PF,\ corr}/p_{\mathrm{T}}$	< 0.15	< 0.15
Missing hits	≤ 1	≤ 1
Conversion vertex fit prob.	$< 10^{-6}$	$< 10^{-6}$

Table 18: Muon ID requirements for the Tight ID working point.

Variable	Cut
isGlobalMuon	True
isPFMuon	True
$\chi^2/ndof$ (global fit)	< 10
Muon chamber hits in global fit	> 0
Muon stations with muon segments	> 1
d_{xy} (from tracker, wrt primary vertex)	< 2 mm
d_z (from tracker, wrt primary vertex)	< 5 mm
Valid pixel hits (tracker track)	> 0
Tracker layers with hits	> 5
$I_{PF,\ corr}/p_{\mathrm{T}}$	< 0.12

Table 19: Data to simulation scale factors for electron (upper) and muon (lower) identification requirements in various η ranges.

electron p_T	$0.0 < \|\eta\| < 0.8$	$0.8 < \|\eta\| < 1.442$	$1.556 < \|\eta\| < 2.0$	$2.0 < \|\eta\| < 2.5$
20 - 30	1.005 ± 0.003	0.981 ± 0.003	0.980 ± 0.005	1.017 ± 0.006
30 - 40	1.004 ± 0.001	0.991 ± 0.001	0.992 ± 0.002	1.019 ± 0.003
40 - 50	1.008 ± 0.001	0.994 ± 0.001	1.004 ± 0.002	1.005 ± 0.001
50 - 200	1.008 ± 0.001	0.999 ± 0.001	1.006 ± 0.003	1.009 ± 0.002

muon p_T	$0.0 < \|\eta\| < 0.8$	$0.8 < \|\eta\| < 2.1$	$2.1 < \|\eta\| < 2.4$
20 - 40	1.0043 ± 0.0004	1.0074 ± 0.0005	1.022 ± 0.001
40 - 100	1.0012 ± 0.0004	1.0043 ± 0.0004	1.014 ± 0.001

D Extra plots

This section contains additional graphs with data to simulation comparisons. Figure 28 displays the number of events in each btag category after full selection. Distributions of the p_{T} after preselection cuts are given in Figures 29 and 30 for the leading and subleading lepton, for electrons and muons. In Figure 31 for the leading and subleading jet. In addition, the reconstructed number of good vertices in data and in reweighed simulation is depicted in Figure 9 for the electron and muon channels combined.

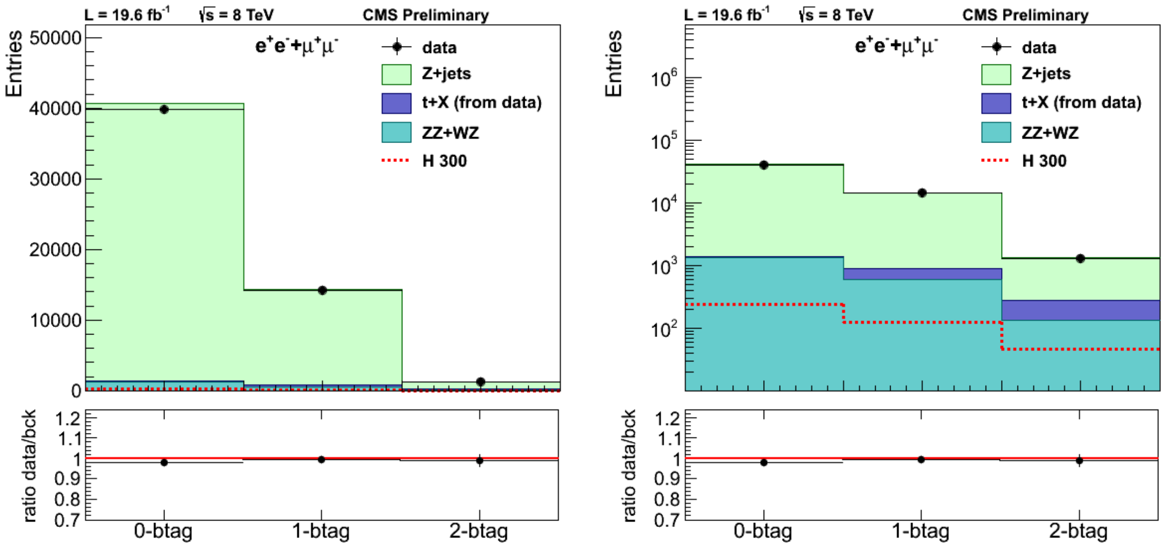

Figure 28: Number of events in each btag category after full selection, for the electron and muon channel combined, in linear (left) and logarithmic scales (right). Dots indicate data, pale green histogram corrected Z+jets simulation, light blue simulated diboson background and dark blue $t\bar{t}$ events from data (which includes single top, WW, $Z \to \tau^+\tau^-$+jets).

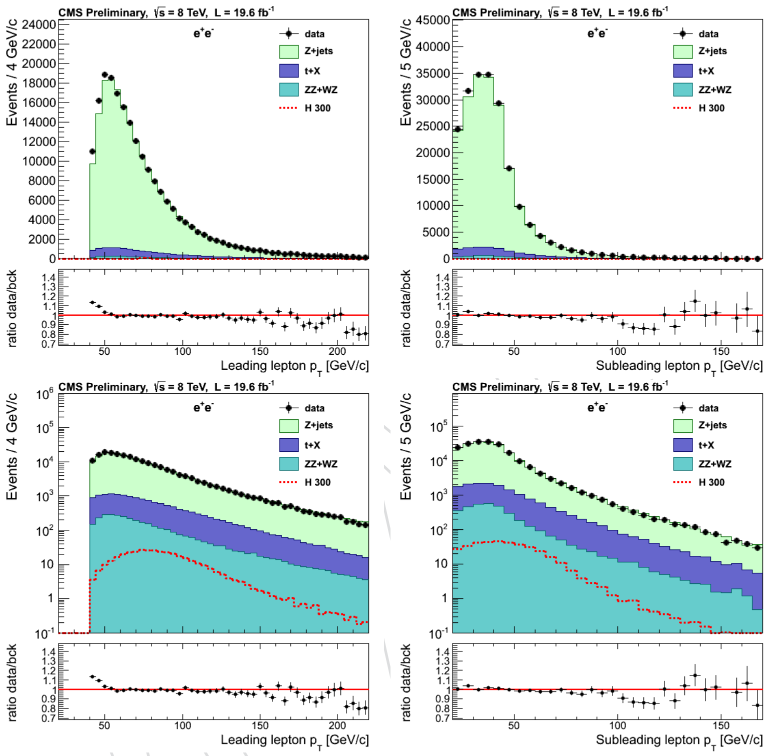

Figure 29: Distributions of the p_T –in linear (upper) and logarithmic scales (lower)– of the leading (left) and subleading electron (right) after preselection cuts. Dots indicate data, pale green histogram corrected Z+jets simulation, light blue simulated diboson background and dark blue $t\bar{t}$ events from data (which includes single top, WW, $Z \to \tau^+\tau^-$+jets).

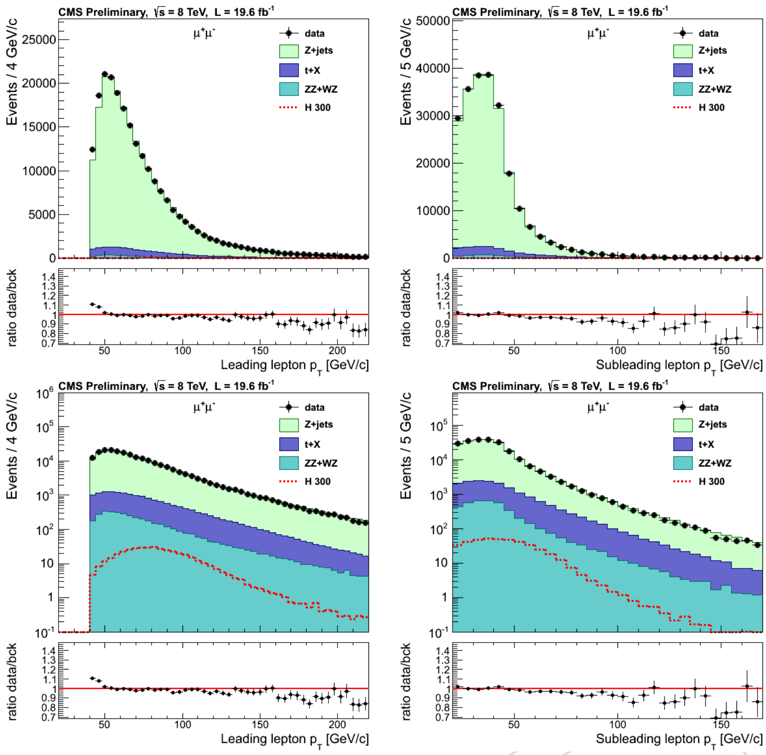

Figure 30: Distributions of the p_T –in linear (upper) and logarithmic scales (lower)– of the leading (left) and subleading muon (right) after preselection cuts. Dots indicate data, pale green histogram corrected Z+jets simulation, light blue simulated diboson background and dark blue $t\bar{t}$ events from data (which includes single top, WW, $Z \to \tau^+\tau^-$+jets).

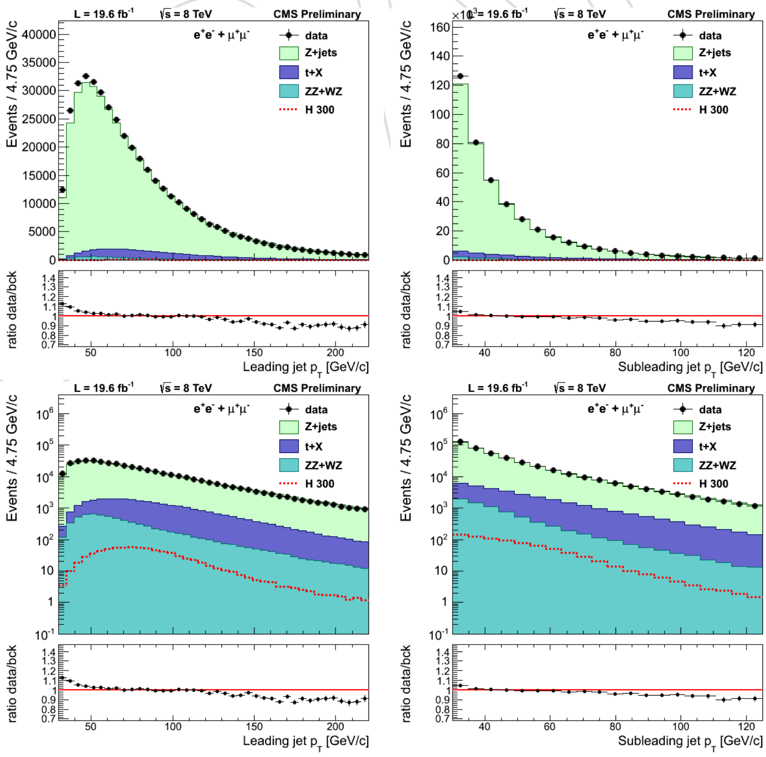

Figure 31: Similar distributions for the leading (left) and subleading jet (right).

E Checks on the likelihood discriminant

The lower-right plot in Figure 5 shows a discrepancy at low LD values. To identify the source of this discrepancy and quantify the impact on the signal, we have studied the distributions of the helicity angles before the LD cut. The overall agreement is very good in all the angles, except in the $\cos\theta^*$ distribution for Z+jets events at $|\cos\theta^*| > 0.85$. As a cross-check, Figure 32 presents the LD distribution applying the cut $|\cos\theta^*| < 0.85$, compared to the original LD distribution. After this cut, Z+jets events are rejected with a minimal impact on the signal efficiency, less than 0.5%, and the agreement of the MC with data is significantly improved.

As an alternative cross-check, rather than cutting in $|\cos\theta^*|$, we have weigthed the Z+jets MC to correct for the improper behavior at $|\cos\theta^*| > 0.85$. The resulting distributions of $\cos\theta^*$ and LD, displayed in Figure 33, show a good agreement of the MC with data, in particular in the LD distribution.

This study demonstrates that the disagreement at low LD values is due to a bad modeling of the $\cos\theta^*$ distribution of Z+jets events at $|\cos\theta^*| > 0.85$, which has a negligible impact on the signal, giving confidence in the analysis.

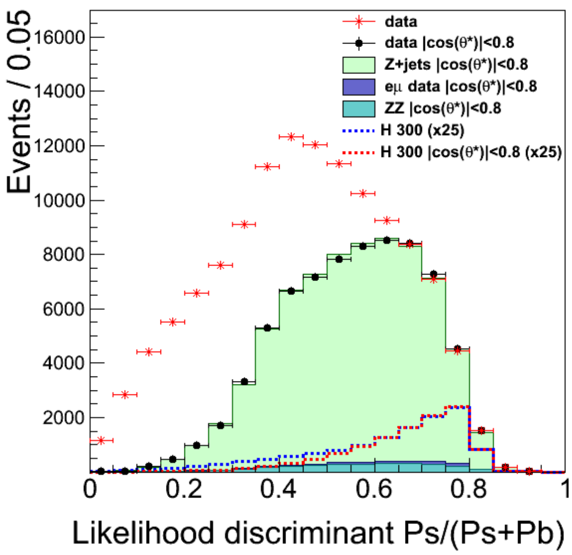

Figure 32: LD distribution for data (black dots), background (coloured histrograms), and signal (dashed red line, $\times$25) events that pass the cut $|\cos\theta^*| < 0.85$. Uncut distributions for data (red dots) and signal (dashed blue line, $\times$25) are also displayed for comparison.

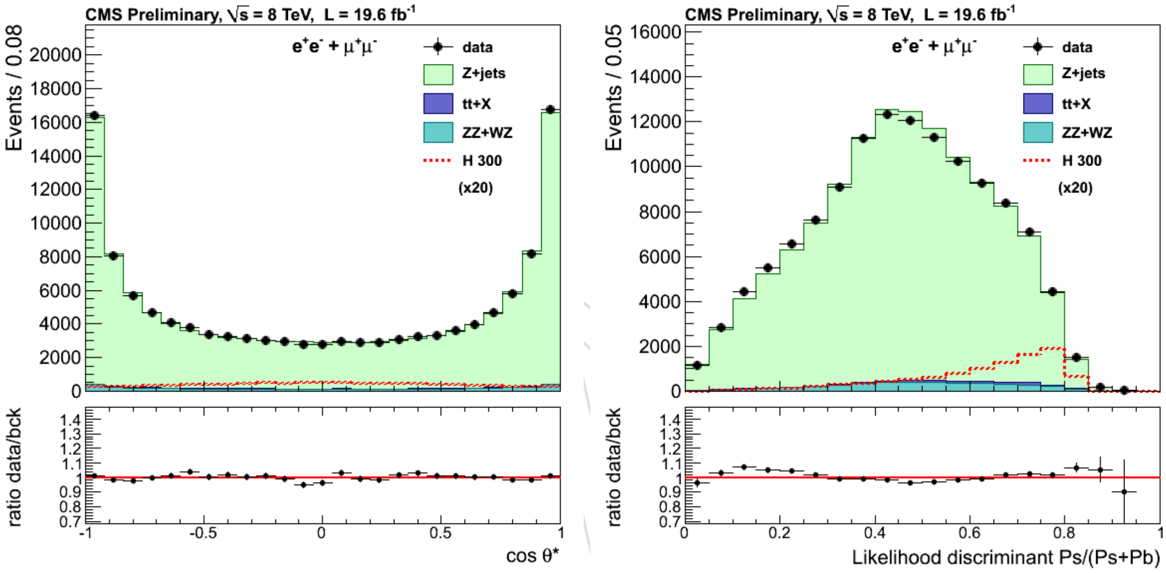

Figure 33: $\cos\theta^*$ and LD distributionis for data (balck dots), background (coloured histrograms), and signal (dashed red line, $\times 20$) events. The Z+jets MC is weighted to match the $\cos\theta^*$ distribution in data.

F Expected signal and background events per btag category

Tables 20, 21, and 22, list the numbers of signal and background events expected for 19.6 fb^{-1} in the mass range $[M_{\mathrm{H}} - 6\%, M_{\mathrm{H}} + 10\%]$ in the three btag categories, separately for the $\mu^+\mu^- jj$ and $\mathrm{e}^+\mathrm{e}^- jj$ channels (denoted $\mu\mu$ and ee, respectively).

Table 20: Expected yields in the 0-btag category.

M_{H} (GeV/c^2)	signal		Z+jets		eμ data		diboson		total background	
	$\mu\mu$	ee	$\mu\mu$	ee	$\mu\mu$	ee	$\mu\mu$	ee	$\mu\mu$	ee
250	90.0	80.4	6160.5	5312.2	24	19	201.7	175.6	6386.3	5506.7
300	90.0	80.6	3334.3	2800.3	11	9	121.1	106.6	3466.6	2915.7
400	82.6	73.5	1254.4	1065.9	1	0	55.9	49.3	1310.9	1115.6
500	33.4	30.2	429.0	381.9	1	1	23.9	20.4	454.0	403.2
600	11.9	10.5	179.3	152.3	0	0	11.3	10.8	190.6	163.2

Table 21: Expected yields in the 1-btag category.

M_{H} (GeV/c^2)	signal		Z+jets		eμ data		diboson		total background	
	$\mu\mu$	ee	$\mu\mu$	ee	$\mu\mu$	ee	$\mu\mu$	ee	$\mu\mu$	ee
250	44.7	40.1	2124.7	1779.0	87	68	89.7	74.2	2301.2	1921.4
300	46.8	40.8	1174.5	987.0	33.0	25	60.8	49.1	1268.3	1062.1
400	45.0	40.8	459.8	406.7	6	5	26.9	24.1	492.9	435.7
500	18.9	17.0	181.1	155.8	1	0	13.9	10.1	195.5	166.3
600	7.0	6.4	80.9	61.4	0	0	6.5	5.5	87.4	66.9

Table 22: Expected yields in the 2-btag category.

M_{H} (GeV/c^2)	signal		Z+jets		eμ data		diboson		total background	
	$\mu\mu$	ee	$\mu\mu$	ee	$\mu\mu$	ee	$\mu\mu$	ee	$\mu\mu$	ee
250	15.6	14.8	180.9	138.6	42	33	18.7	16.4	241.7	188.0
300	18.5	16.0	91.2	70.9	28	22	12.2	11.7	131.4	104.6
400	19.8	16.8	32.2	24.6	1	0	7.0	5.3	39.7	30.4
500	8.2	7.5	9.6	8.9	0	0	2.7	2.5	12.3	11.4
600	3.0	2.8	5.6	4.5	0	0	1.7	1.5	7.3	6.0

G Determination of $t\bar{t}$ background from data

In the analysis, the $t\bar{t}$ background is estimated from data. Additional plots supporting the robustness of the procedure are presented below. The comparison of $e^{\pm}\mu^{\mp}$ and $(e^{+}e^{-} + \mu^{+}\mu^{-})$ dsitributions using Powheg + Pythia top MC shows an excellent agreement, as depicted in Figure 34 for several variables after different steps of the selection. A similar agreement is observed in Figure 35, which compares the 2012 $e^{\pm}\mu^{\mp}$ data to Powheg + Pythia top MC. Figure 36 displays the MET significance distribution for dilepton data compared to the sum of Drell-Yan Monte Carlo plus $e^{\pm}\mu^{\mp}$ data for events with and two (1 JPM + 1 JPL) btags, and the dijet invariant mass (right) for $e^{+}e^{-} + \mu^{+}\mu^{-}$ and $e^{\pm}\mu^{\mp}$ data for events outside the leptonic Z mass window, show again very good agreement.

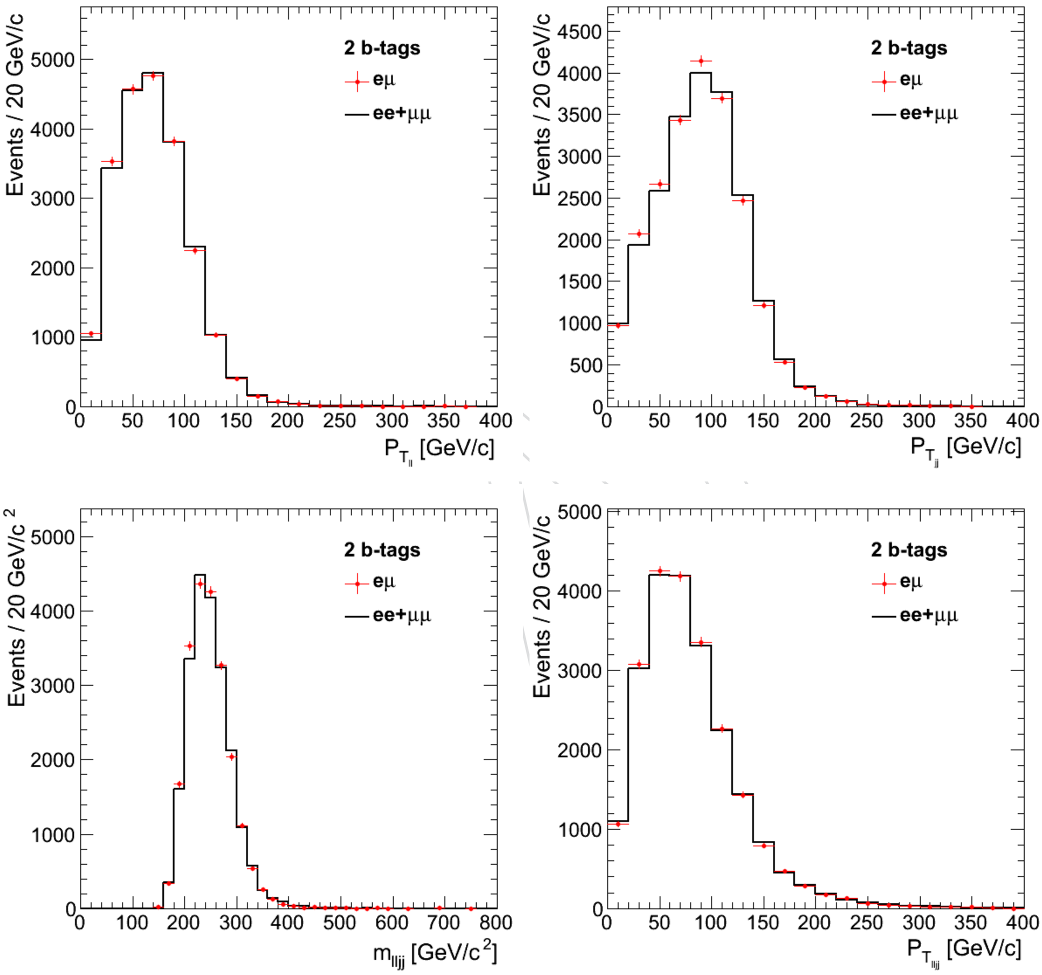

Figure 34: Powheg + Pythia top MC $e^{\pm}\mu^{\mp}$ to $(e^{+}e^{-} + \mu^{+}\mu^{-})$ comparison for several variables after different steps of the selection, as specified in the legends. Top: dilepton (left) and dijet transverse momentum (right). Bottom: dilepton + dijet "Higgs" invariant mass (left) and transverse momentum (right).

Next, the data-driven evaluation of the $t\bar{t}$ background is compared to an alternative method based on top simulation only. Figure 37 compares the previous $e^{\pm}\mu^{\mp}$ data distributions to the prediction of Powheg + Pythia top MC normalized to the NLO $t\bar{t}$ cross-section. The gray area represents the systematic error (including luminosity, lepton trigger and ID efficiencies, b-tagging efficiency, mistag efficiency, and pile-up uncertainties; no contribution from normal-

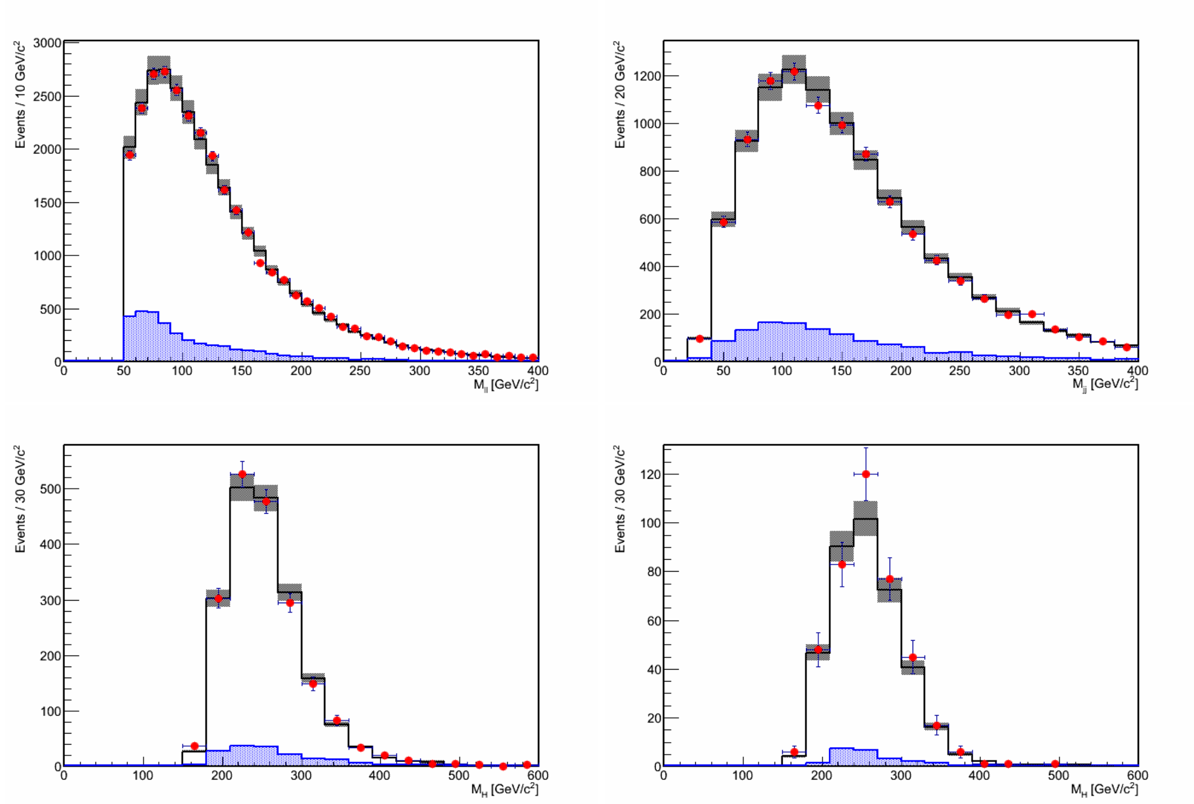

Figure 35: Comparison of 2012 $e^{\pm}\mu^{\mp}$ data to Powheg + Pythia top MC, corresponding to an integrated luminosity of 19.6 fb^{-1}. Red dots are $e^{\pm}\mu^{\mp}$ data; white histogram top Monte Carlo; blue histogram other small backgrounds. Top: dilepton invariant mass (left) and dijet invariant mass (right). Bottom: "Higgs" invariant mass for events with 1 JPL b-tag (left), and two (1 JPM + 1 JPL) b-tags and MET significance < 10 (right).

ization) of the MC prediction. With the 19.6 fb^{-1}, the statistical errors of the $e^{\pm}\mu^{\mp}$ data points compare well to the size of the gray boxes. In addition, the $t\bar{t}$ MC underestimates the normalization of the $e^{\pm}\mu^{\mp}$ data by 20% before b-tagging (12% for events with 2 b-tagged jets). Based on this comparison we choose to use the data-driven estimation.

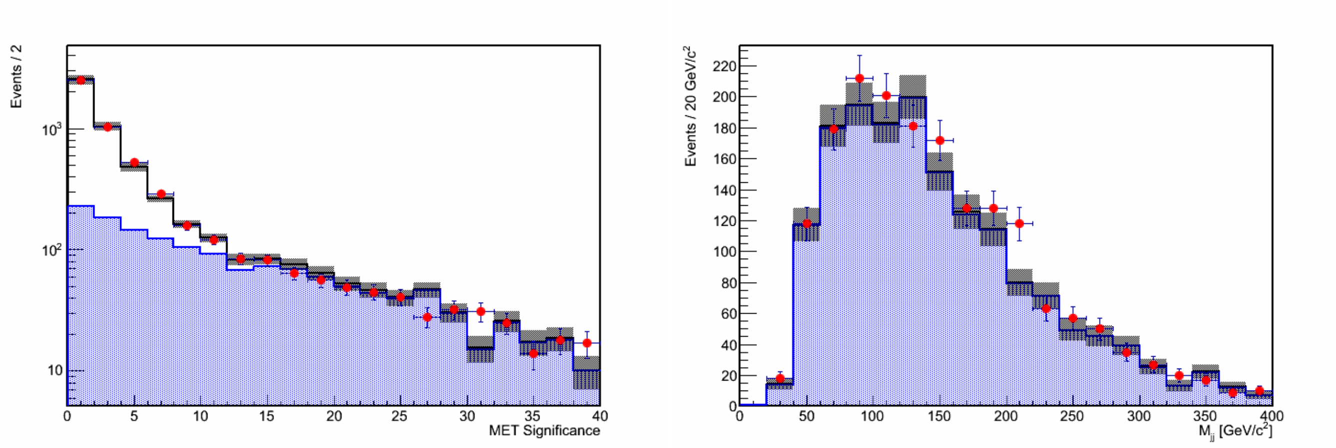

Figure 36: MET significance distribution for dilepton data compared to the sum of Drell-Yan Monte Carlo plus $e^{\pm}\mu^{\mp}$ data for events with two btags (left). Dijet invariant mass (right) for $e^{+}e^{-} + \mu^{+}\mu^{-}$ and $e^{\pm}\mu^{\mp}$ data for events outside the leptonic Z mass window, with two b-tags, and MET significance > 8. Other cuts are detailed in the text. Red dots are $e^{+}e^{-} + \mu^{+}\mu^{-}$ data; white histogram Drell Yan Monte Carlo; blue histogram $e^{\pm}\mu^{\mp}$ data (plus other small backgrounds).

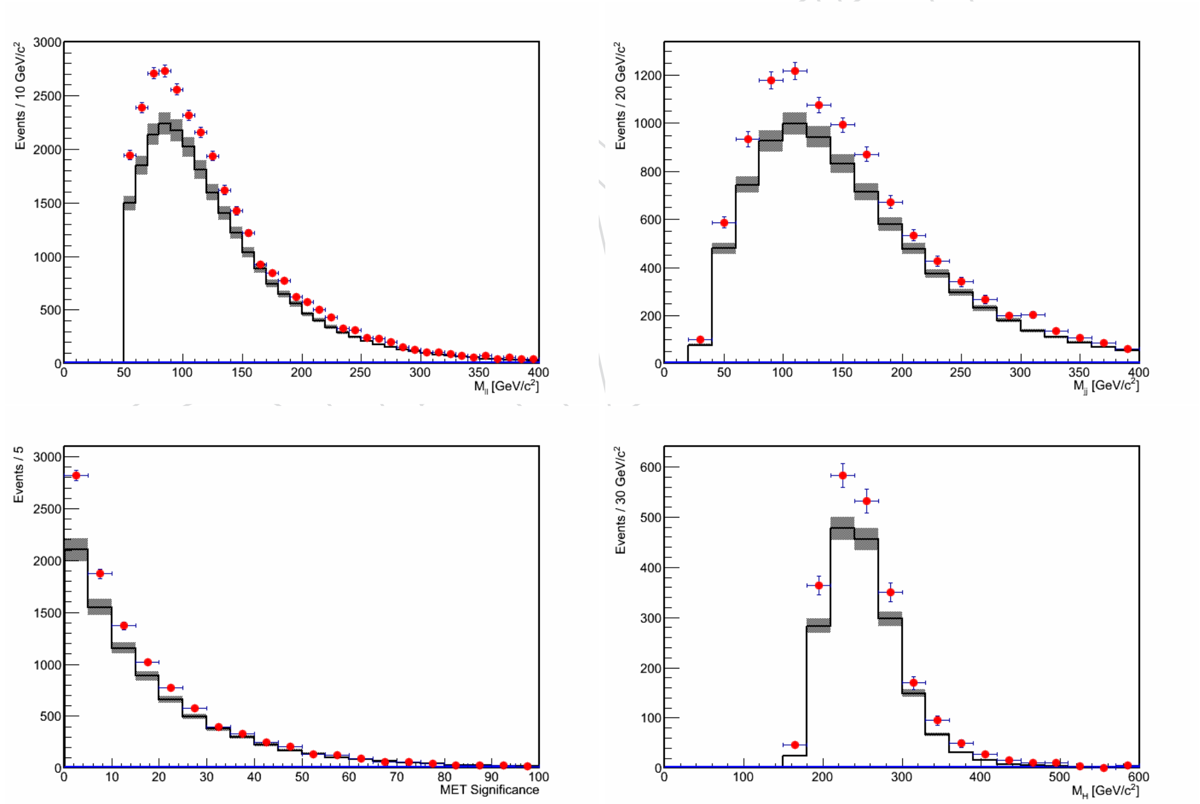

Figure 37: Comparison of 2012 $e^{\pm}\mu^{\mp}$ data to Powheg + Pythia top MC normalized to the $t\bar{t}$ NLO cross-section. Red dots are $e^{\pm}\mu^{\mp}$ data; white histogram top Monte Carlo. Top: dilepton invariant mass (left) and dijet invariant mass (right). Bottom: MET significance (left), and "Higgs" invariant mass (right).

H Systematic uncertainties on the signal

The systematic uncertainty on the signal are listed in Tables 23 (muon channel) and 24 (electron channel), for various M_{H} values, for the three btag categories.

Table 23: Systematic uncertainty on the signal in the muon channel.

M_{H} (GeV/c^2)	0-btag		1-btag		2-btag	
	$1\sigma_{UP}$ (%)	$1\sigma_{DOWN}$ (%)	$1\sigma_{UP}$ (%)	$1\sigma_{DOWN}$ (%)	$1\sigma_{UP}$ (%)	$1\sigma_{DOWN}$ (%)
200	-3.2	1.5	5.8	-1.3	4.0	-6.7
210	-3.4	1.2	4.8	-1.9	8.5	-2.5
220	-3.1	1.7	4.5	-1.7	6.8	-6.1
230	-3.4	1.8	4.8	-2.1	7.4	-5.3
250	-2.9	2.1	3.8	-2.4	6.3	-5.5
275	-3.4	1.5	4.5	-1.0	6.1	-5.5
300	-3.6	1.4	4.6	-0.69	6.8	-5.7
350	-3.8	1.7	4.7	-0.84	6.7	-6.1
375	-3.7	1.7	5.0	-0.31	5.2	-7.5
400	-3.9	1.6	4.5	-0.74	6.8	-5.7
425	-4.1	1.6	5.1	-0.59	5.9	-5.8
450	-4.1	1.8	4.0	-1.1	8.1	-5.0
475	-3.9	1.8	4.1	-0.6	7.0	-6.5
500	-3.6	2.1	3.6	-0.97	7.1	-6.7
525	-4.1	2.0	4.8	-0.65	6.4	-7.1
550	-3.6	1.9	3.5	-0.87	6.9	-5.6
575	-4.4	1.8	4.9	-0.78	6.7	-5.7
600	-4.3	1.9	4.4	-1.3	7.8	-4.9

Table 24: Systematic uncertainty on the signal in the electron channel.

M_{H} (GeV/c^2)	0-btag		1-btag		2-btag	
	$1\sigma_{UP}$ (%)	$1\sigma_{DOWN}$ (%)	$1\sigma_{UP}$ (%)	$1\sigma_{DOWN}$ (%)	$1\sigma_{UP}$ (%)	$1\sigma_{DOWN}$ (%)
200	-3.4	1.8	3.9	-3.7	12	-0.18
210	-3.5	1.2	5.4	-1.1	6.9	-5.5
220	-2.9	1.9	4.1	-2.0	7.0	-7.2
230	-3.6	1.4	4.9	-1.9	8.7	-3.5
250	-2.9	2.2	4.0	-2.4	5.1	-6.2
275	-3.5	1.5	4.7	-1.3	6.3	-4.6
300	-3.9	1.5	5.9	-0.26	5.9	-7.7
350	-3.9	1.5	4.7	-0.41	7.1	-6.5
375	-3.9	1.8	4.5	-1.1	7.5	-5.7
400	-3.9	1.9	4.0	-1.1	8.2	-6.0
425	-4.0	1.8	4.8	-0.67	6.9	-6.6
450	-3.9	1.5	3.8	-0.43	7.8	-5.3
475	-4.3	1.8	5.2	-0.54	6.1	-6.2
500	-4.1	2.0	5.2	-0.83	5.8	-6.7
525	-4.0	2.0	3.8	-1.3	8.1	-5.5
550	-4.0	1.8	4.5	-1.1	6.2	-5.1
575	-4.0	1.9	4.1	-0.67	7.1	-6.2
600	-4.4	1.8	5.2	-0.68	6.7	-6.1

I Mass distributions for the electron and muon channels

The $M_{\ell\ell jj}$ distributions, depicted in Figure 38 for the electron and muon channels, display an excellent agreement both in the m_{jj} sideband and signal regions.

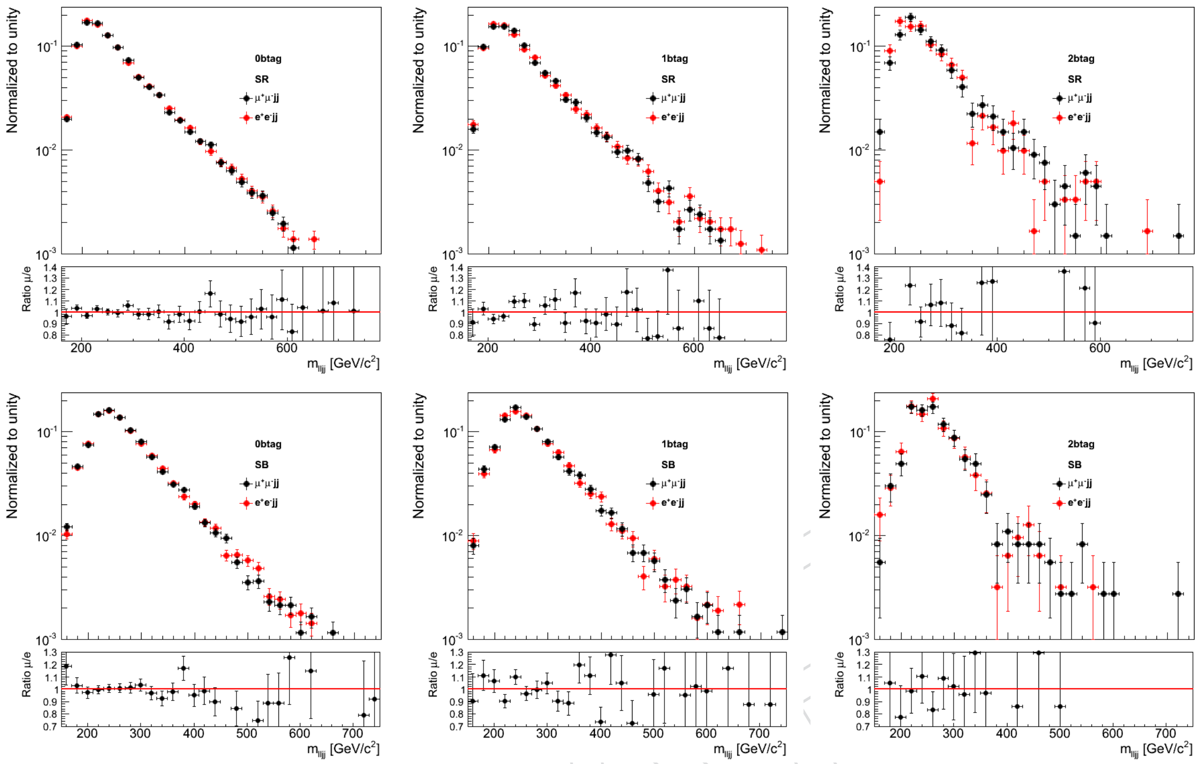

Figure 38: Mass distributions of the $\ell^+\ell^- jj$ system for events in the electron and muon channels: data in the m_{jj} (top) signal and (bottom) sideband regions. From left to right, plots correspond to the 0-, 1-, and 2-btag categories.

J Limit Cross Checks

Another approach, referred to as *cut-and-count* analysis, uses only the number of events selected with a reconstructed Higgs mass in the window $[M_H - 6\%, M_H + 10\%]$. The Higgs cross section limit is determined from the expected number of signal and background events passing the selections s and b respectively. The results shown in Figure 39 are compatible with the full results.

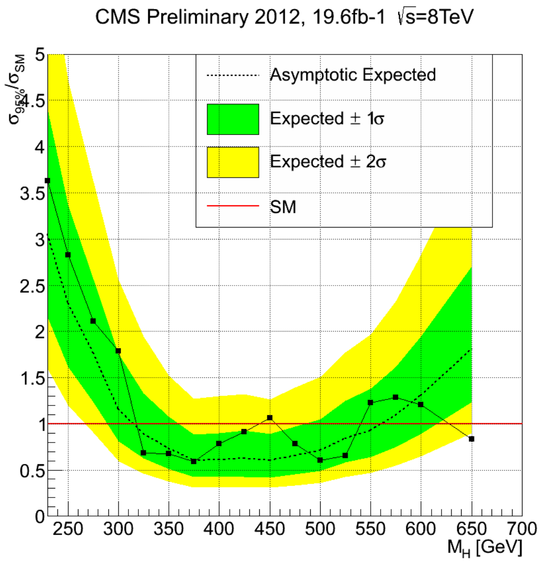

Figure 39: Observed (solid) and expected (dashed) 95% CL upper limit on the ratio of the production cross section to the SM expectation for the Higgs boson obtained using the *cut-and-count* technique, which integrates the mass distibutions in a range $[M_H - 6\%, M_H + 10\%]$ around each Higgs mass hypothesis. The 68% and 95% ranges of expectation for the background-only model are also shown with green and yellow bands, respectively. The solid line at 1 indicates the expectation for a SM-Higgs-like boson.

K Cross Checks requested at Approval

The following cross checks were requested during approval:

1. Take the Z+jets MC sample and define the scale factor based on the overall number of events after the preselection in the signal dijet mass window with respect to the sideband mass windows. Apply this constant scale factor to the differential distribution of 4-body mass in the Z+jets events in the sideband and see if you reproduce that for the signal region in the entire mass range.
2. Compare the 4-body mass distributions for the lower and upper sideband in the data and see if the ratio is constant with the 4-body mass.
3. Make a technical check of the last steps of the analysis, just to be safe.
4. Make the combination with 7 TeV as published (this was a condition at the pre-approval in fact).
5. Consider stopping the analysis at 600 GeV in light of the concerns.

K.1

As can be seen in Figure 40 the tail is basically the same, implying that there is no issue in the shape due to jet merging or so. In the low mass region there is a clear difference, but this has already been studied in the past and it is due to the bias from the mJJ selection.

However, this is not a closure test as one may think on such: if it is intended to validate our analysis methodology, it is not the proper test, since this is not what we do in the analysis (more below). If it is to check that the shapes are the same, they are not... and we know that: the mllJJ and mJJ variables are not fully decoupled (specially at low masses) and therefore there are differences.

It should be added that in our analysis we are not taking the shape of the SB for anything except to validate the MC expectations. The shape in the SB does not have any influence in the result. It has been relevant of course in the decision to unblind the analysis, but only that. We are not using it in any way to infer the shape in the SR for Z+jets (that is what the test above seems to suggest). Only the normalization in the SB has some impact on the result.

In our analysis, we are not assuming that the shape from the SB is able to reproduce the SR. Even if at high masses they agree (because the requirement on mJJ has smaller influence), we are not using that information. We are extracting the expected shape from the same SR but the MC and we are assuming that MC reproduces the SR as well as the SB. In fact today we know that the MC reproduces the shape in BOTH SB, so assuming it also works in the SR is the natural thing to do. We have no reason to think that there is something in the Z-peak region affecting Z+jets that does not affect any of the two SB, one at lower masses and the other at higher masses.

Furthermore (last but not least), we did not claim that the shape in the MC is perfectly reproduced and we have a systematic uncertainty. As shown in the approval talk, we quote a large systematic on the shape that covers by far any discrepancy observed in the SB regions (plots this morning). Recall the systematic is really large at high masses.

K.2

Figure 41 to 44 show the sideband data compared to the background prediction separately for the left and right sideband. While the background shapes are noticeably different between the

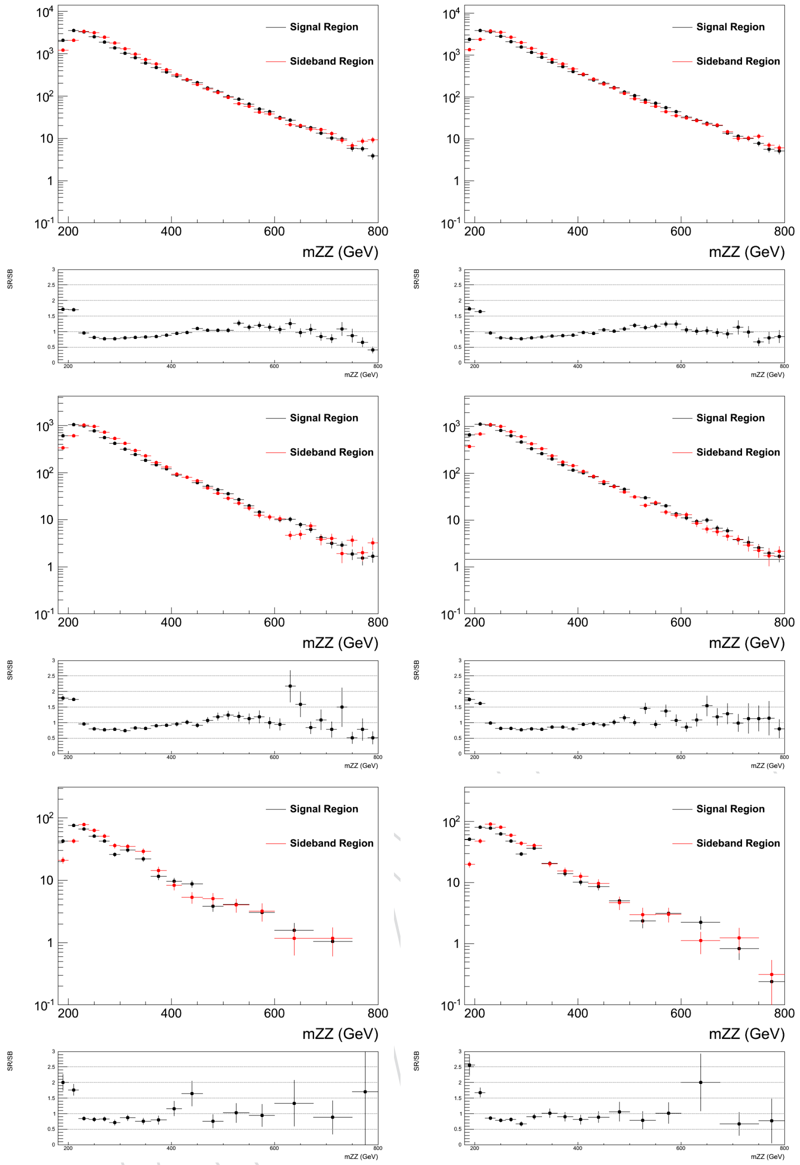

Figure 40: Mass distributions of the $\ell^+\ell^- jj$ system for events in the simualted sideband and signal regions for the elctron (left) and muon (right) channels. From top to bottom, plots correspond to the 0-, 1-, and 2-btag categories.

left and right sideband, both agree well between data nad simulation, giving conifdence that the description is similarly good in the signal region.

K.3

We have three independent analyses (different codes, ntuples, etc.) which agree well at the sub-percent level, in the numbers of events and shapes of the distributions. We have also checked the final limits, calculated both with the official combine tool and with an independent home-made code, and give consistent results. These checks have been reported in HZZ meetings and at the pre-approval session.

We are confident that no bug is present that gives visible effects.

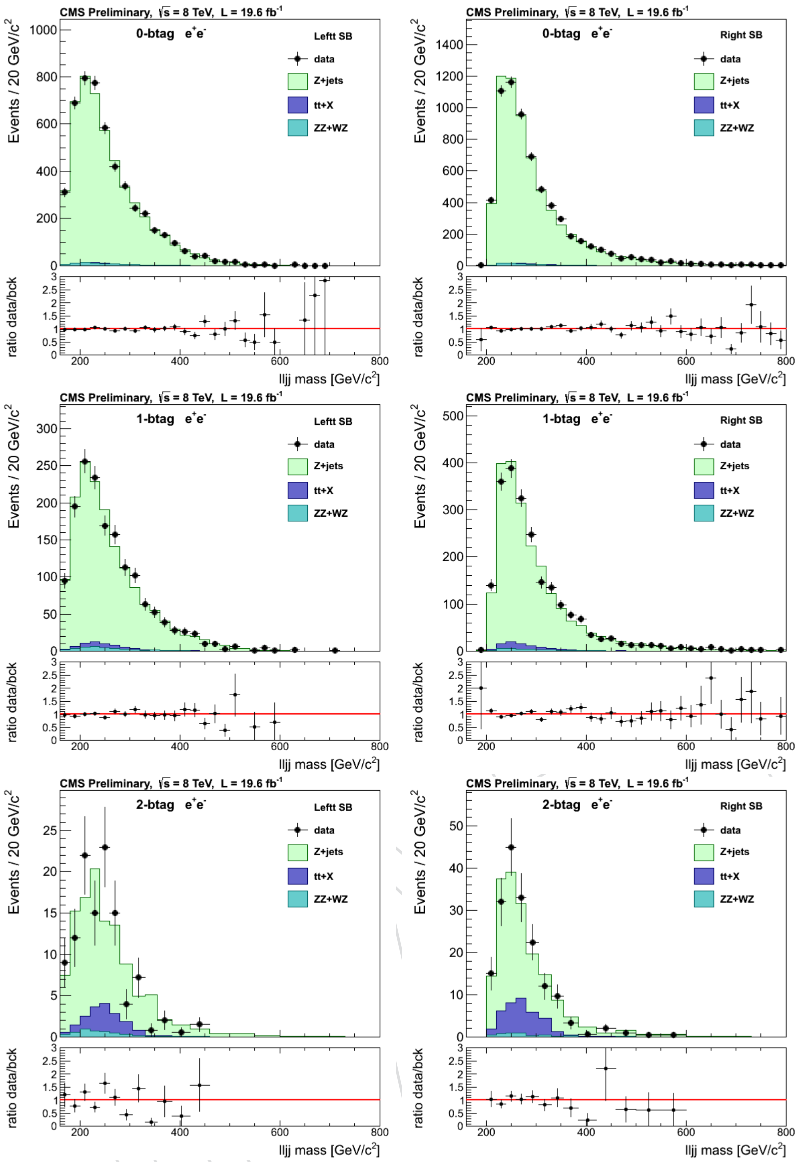

Figure 41: Mass distributions of the $\ell^+\ell^- jj$ system for events in the left (left) and right (right) sideband regions in the electron channel. From top to bottom, plots correspond to the 0-, 1-, and 2-btag categories. The dots are data, pale green histogram corrected Z+jets simulation, light blue simulated diboson background and dark blue $t\bar{t}$ events from data (which include single top, WW, $Z \to \tau^+\tau^-$+jets).

K.4

see section 7

K.5

This has been addressed in the PAS. For internal documentation we keep the wider range in this note.

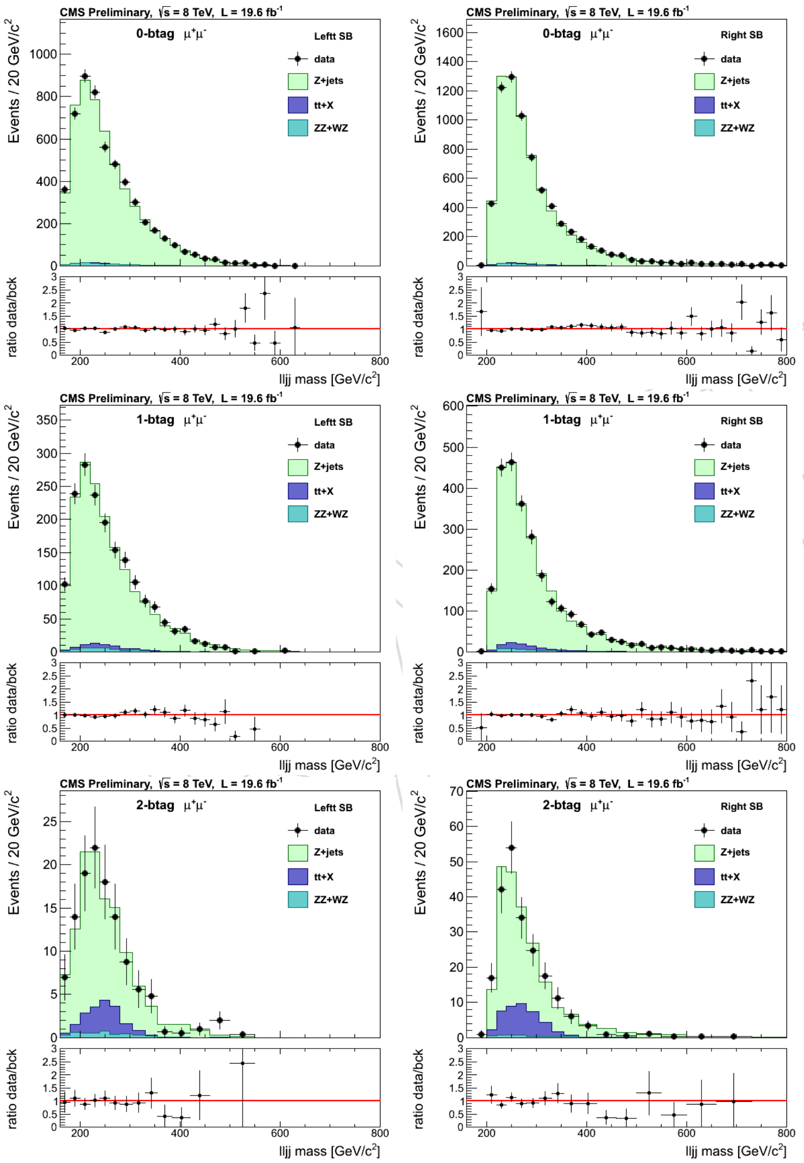

Figure 42: Same Figure 41 but in themuon channel.

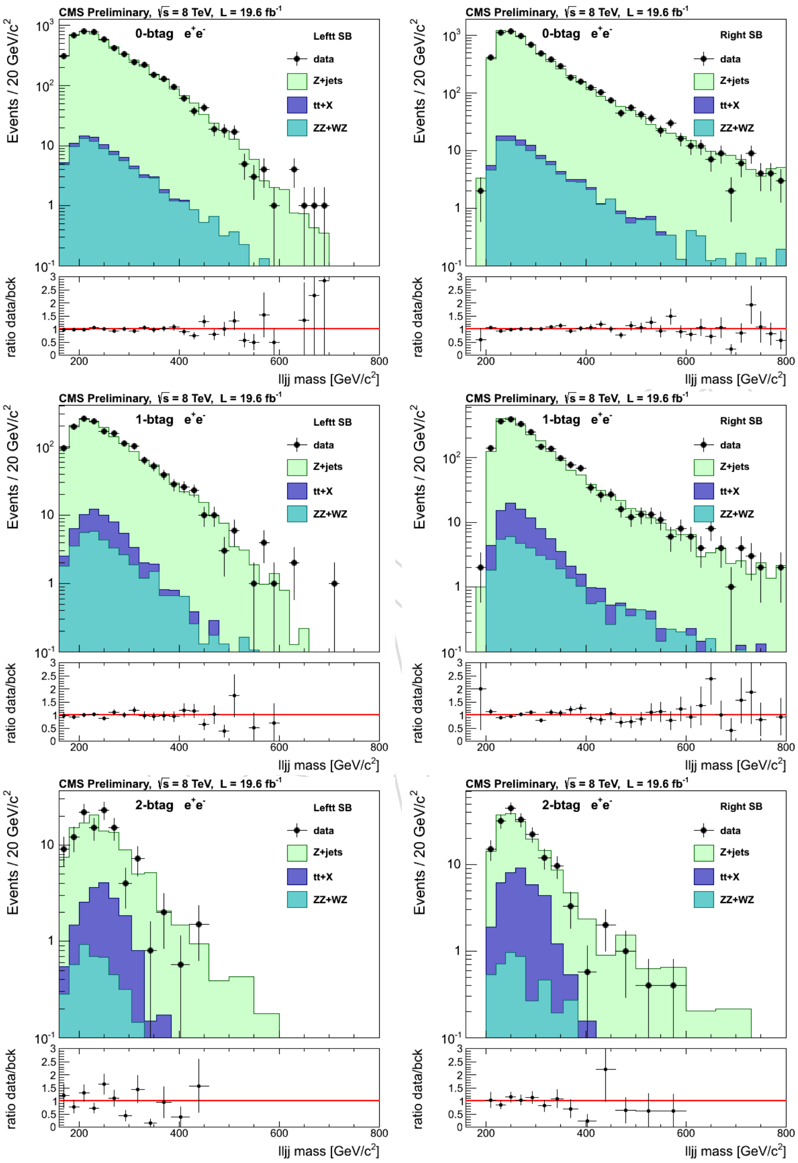

Figure 43: Same Figure 41 but in themuon channellogarithmic scale.

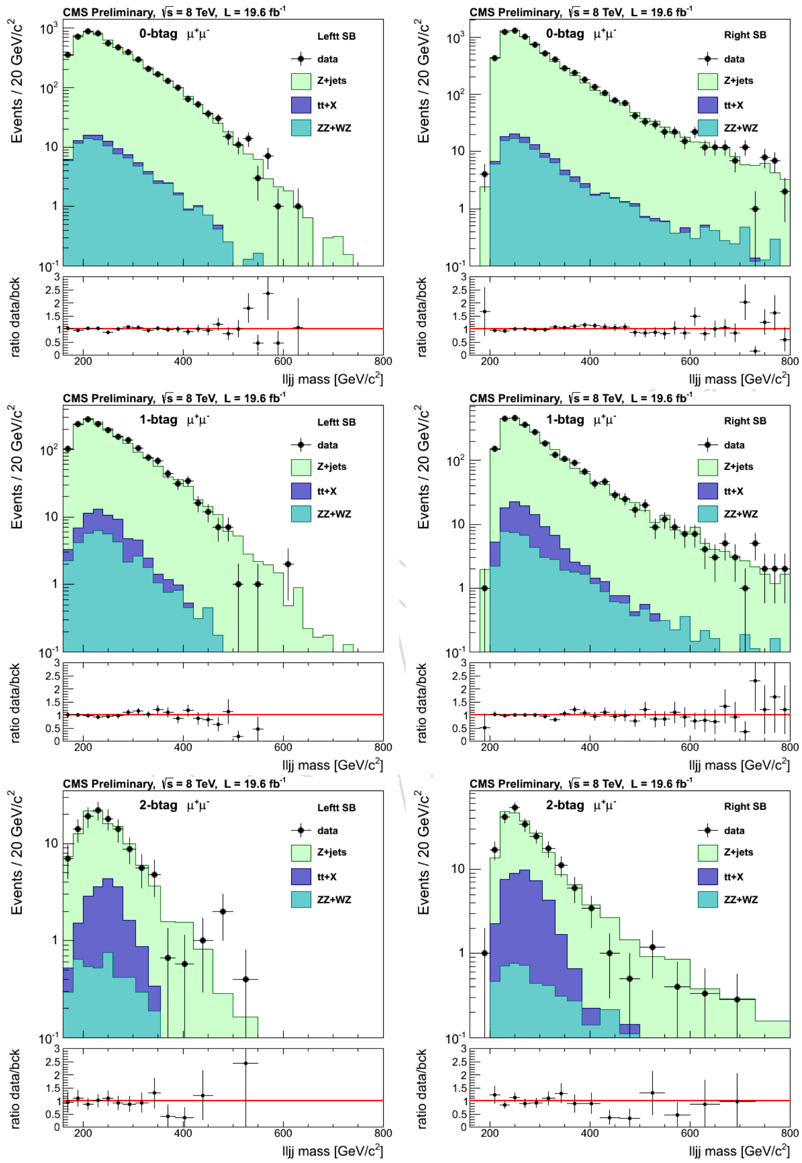

Figure 44: Same Figure 42 but in themuon channellogarithmic scale.